# Achieving ultrahigh fatigue resistance in AlSi10Mg alloy by additive manufacturing

Chengyi Dan, Yuchi Cui, Yi Wu, Zhe Chen, Hui Liu, Gang Ji, Yakai Xiao, Han Chen, Mingliang Wang, Jun Liu, et al.

# Achieving Ultrahigh Fatigue Resistance in AlSi10Mg Alloy by Additive Manufacturing

Chengyi Dan[1,2]†, Yuchi Cui[1]†, Yi Wu[2]†, Zhe Chen[1,2]†*, Hui Liu[3], Gang Ji[4], Yakai Xiao[2], Han Chen[2], Mingliang Wang[1], Jun Liu[2], Lei Wang[2], Yang Li[2], Ahmed Addad[4], Ying Zhou[2], Siming Ma[2], Qiwei Shi[2], Haowei Wang[1,2], Jian Lu[3]*

**Affiliations:**

[1]State Key Laboratory of Metal Matrix Composites, Shanghai Jiao Tong University, Shanghai 200240, PR China

[2]School of Materials Science and Engineering, Shanghai Jiao Tong University, Shanghai 200240, PR China

[3]Department of Mechanical and Biomedical Engineering, City University of Hong Kong, Kowloon, Hong Kong, China

[4]Univ. Lille, CNRS, INRA, ENSCL, UMR 8207 - UMET - Unité Matériaux et Transformations, 59000 Lille, France

*Corresponding author. Email: zhe.chen@sjtu.edu.cn, jianlu@cityu.edu.hk.

† These authors contributed equally to this work.

**Abstract:** Since the first discovery of fatigue phenomenon in the late 1830s, the efforts to fight against fatigue failure have never been stopped by materials scientists and mechanical engineers. Here we report a fatigue immunisation phenomenon in nano-$TiB_2$ decorated AlSi10Mg (NTD-Al) enabled by additive manufacturing. This fatigue immunisation mechanism benefits from the 3D dual-phase cellular nanostructure, which acts as a strong volumetric 3D dislocation nanocage to prevent the localised damage accumulation, thus inhibiting fatigue crack initiation. The intrinsic fatigue strength limit of NTD-Al was proven to be close to its tensile strength through *in situ* fatigue test of a defect-free micro-sample, where sign of neither crack initiation nor accumulated fatigue damages was observed. To demonstrate the practical applicability of this mechanism, the printed bulk NTD-Al achieved

record high fatigue resistance tested by ASTM standard, which was more than double those of other additive manufacturing Al alloys and surpassed those of high-strength wrought Al alloys. A paradigm of achieving high fatigue resistance through additive manufacturing phase engineering has been established from nanoscale structural design to the fabrication of geometrically intricate industrial components, which will be extended to the design and development of other fatigue-resistant metals.

**Main Text:**

Fatigue resistance is a critical design criterion of structural components, as it is estimated that over 80% of engineering failures are due to fatigue[1]. Insufficient fatigue strength of metals has remained an unsolved problem for almost two centuries, where conventional metals exhibit fatigue strength generally lower than half of their tensile strength. In particular for Al alloys, which are the second widely used metals in industry, the typical fatigue strength ratio (fatigue strength limit/tensile strength) is only about 1/3[2]. This leads to a very important fact, but seldom mentioned in industry that for all the moving Al components suffering from cyclic loads, the load efficiency of materials utilisation is roughly estimated to be less than 20%, considering the safety factors and the inhomogeneous stress distribution in engineering components. Despite the metallurgical defects introduced during manufacturing, the intrinsic mechanism for the lower fatigue resistance is the irreversible dislocation slips taking place in particular grains due to the severe heterogeneous strain distribution in polycrystalline metals, therefore enabling localised damage accumulation that initiates fatigue cracks. Recent efforts have shown that through microstructure design, fatigue resistance of metals can be dramatically enhanced, e.g. bone-like nano-laminated substructure arresting fatigue cracks in steel[3], fatigue-induced precipitation strengthening weak grain boundaries in Al alloy[2] and highly oriented nanoscale twins constraining reversible cycling damages in copper[4].

Laser powder bed fusion (LPBF), as one of the most widely used metal additive manufacturing (AM) techniques, is known for its capability of directly fabricating geometrically complex components with free topology optimisation design. It is worth more attention that the rapid cooling rate of LPBF also provides unrivaled material microstructure

designability down to nanoscale. Here we report a fatigue immunisation mechanism in AlSi10Mg alloy fabricated by LPBF AM. We demonstrate that continuous 3D dual-phase cellular nanostructure (3D-DPCN) of the LPBF AM AlSi10Mg alloy is immune to fatigue by inhibiting localised damage accumulation and fatigue crack initiation. This fatigue immunisation mechanism is distinct from the fatigue mechanisms of conventional metals that have been studied for over a century. Through an *in situ* micro-fatigue experiment, it is found that the intrinsic fatigue strength limit ($> 10^7$ cycles) of a defect-free sample is close to its tensile strength, and the post-fatigue sample is observed to be crack-free and absent of localised fatigue damage accumulation, where a fatigue ratio of ~ 0.9 is achieved. As a proof of the fatigue immunisation mechanism in bulk sample, we fabricated a record high fatigue-resistant nano-$TiB_2$-decorated AlSi10Mg (NTD-Al) alloy through optimizing printing defects. The fatigue strength limit of the NTD-Al alloy, following ASTM standards, was the best among all Al alloys including the conventional high-strength wrought Al alloys with limited metallurgical defects, and more than double those of other reported AM Al alloys[2,5-22] (Fig. 1A and B). It is worth mentioning that the NTD-Al alloy has been applied to fabricate large thin-walled structures, including fan blades of aircraft engine designed by virtue of its high fatigue strength, and successfully passed the qualifying fatigue test (Fig. 1C). These findings not only provide a novel path to designing fatigue resistant alloys in metal research community, but also raise a new opportunity to weight reduction by increasing the materials load efficiency of moving components. Combined with the various advantages of 3D printing, such as topological optimisation (Fig. 1D), this work would have everlasting impacts on modern industry in terms

of component weight reduction, and influence future society in terms of low-carbon emission from aircrafts and vehicles with the development and mass application of never-fatigue metals.

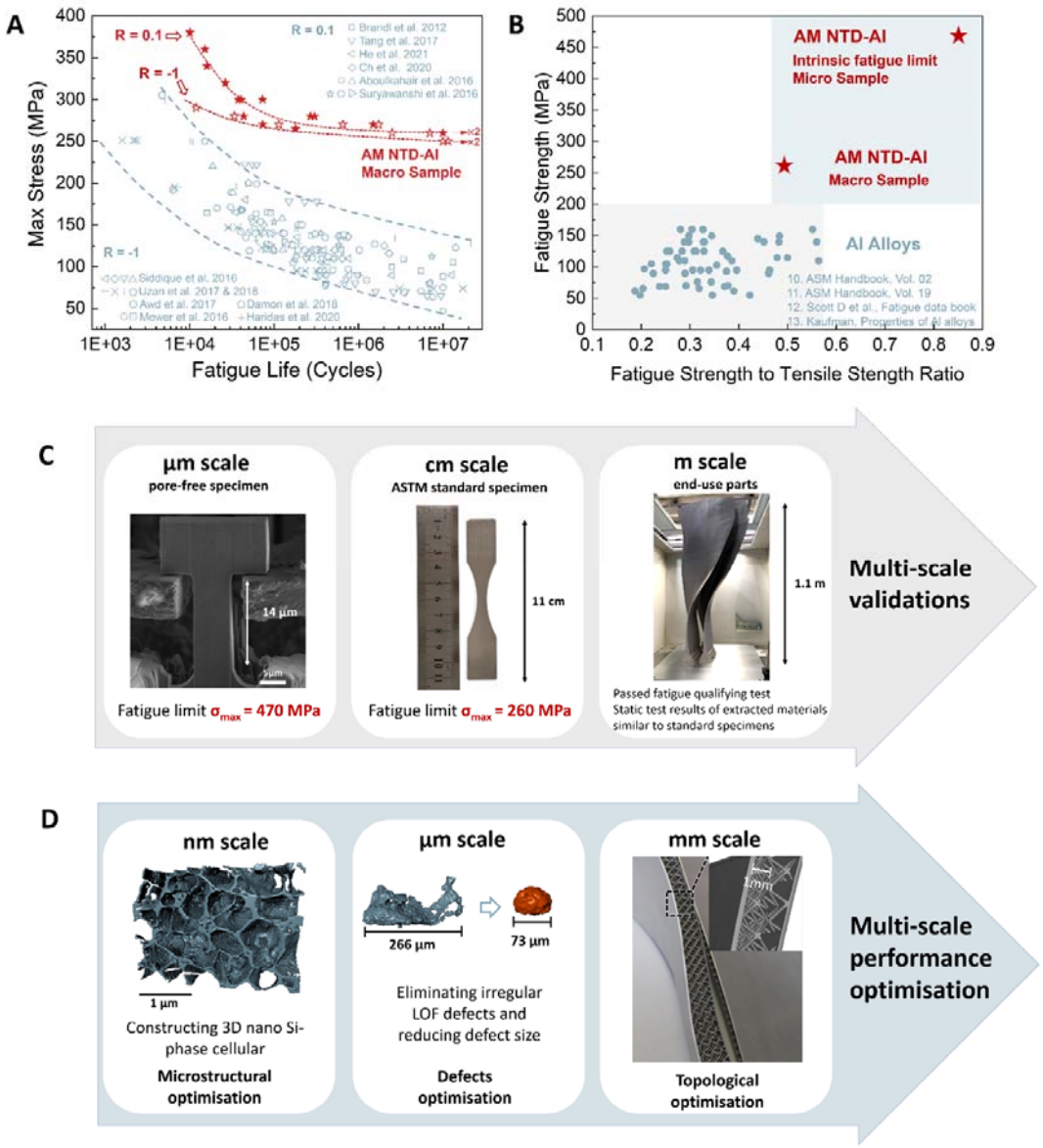


**Fig. 1 Achieving high fatigue strength of the AM NTD-Al alloy.** (A) Number of cycles to failure plotted against the maximum stress of AM NTD-Al (stress ratio (R) = 0.1 and -1), compared with other reported AM AlSi10Mg and AlMgScZr alloys[5-9,14-22]. (B) Fatigue limit to tensile strength ratio vs. fatigue strength of AM NTD-Al, compared with Al alloys, R = -1[2,10-13]. (C) Multi-scale specimen validations for unprecedented fatigue performances. (D) Multi-scale optimisation strategies for performance improvement.

We applied LPBF-AM to fabricate the samples using AlSi10Mg powders decorated with $TiB_2$ nanoparticles[23], as demonstrated in Extended Data Fig. 1. Samples for standard fatigue tests were printed by ProX DMP 200 made by 3D Systems (Extended Data Fig. 2). The optimised powder chemical composition and printing parameters are given in Extended Data Table 1. Micro-computed tomography (μ-CT) analysis was used to investigate the printing defects in the NTD-Al, where uniformly distributed nearly spherical pores were found throughout the sample (Fig. 2A). The widely reported detrimental defects in common AM AlSi10Mg, the irregular shaped lack of fusions (LOFs, often in size of hundreds of micrometers, Extended Data Fig. 3A and B), resulted from the improper fusion between successive tracks or layers due to insufficient energy density[24] were absent in our NTD-Al sample. Electron backscatter diffraction (EBSD) showed a quasi-equiaxed grain morphology with an average size of approximately 2–3 μm (Fig. 2B). Further characterisation revealed a typical DPCN that consisted of a network of solidification cellular structure with an average diameter of ~ 500 nm and α-Al inside the cellular structure (Fig. 2C). Continuous 3D-DPCN were revealed by the tomographic reconstruction of backscattered electron (BSE) images from sections sliced by focused ion beam (FIB) (Fig. 2D). Close-up transmission electron microscopy (TEM) images showed that the cellular structure was composed of polycrystalline Si grains of several to tens of nanometers in size and random crystallographic orientations (Fig. 2E and F). The main component of the 3D-DPCN was Si phases containing a few $TiB_2$ nanoparticles that could be observed in the energy dispersive spectroscopy (EDS) maps (Fig. 2F and G). EOS M280 was also used to print NTD-Al samples, showing no notable difference

compared to ProX DMP 200 (Extended Data Fig. 3 and 4), validating the applicability of our design strategy in different printing scenarios.

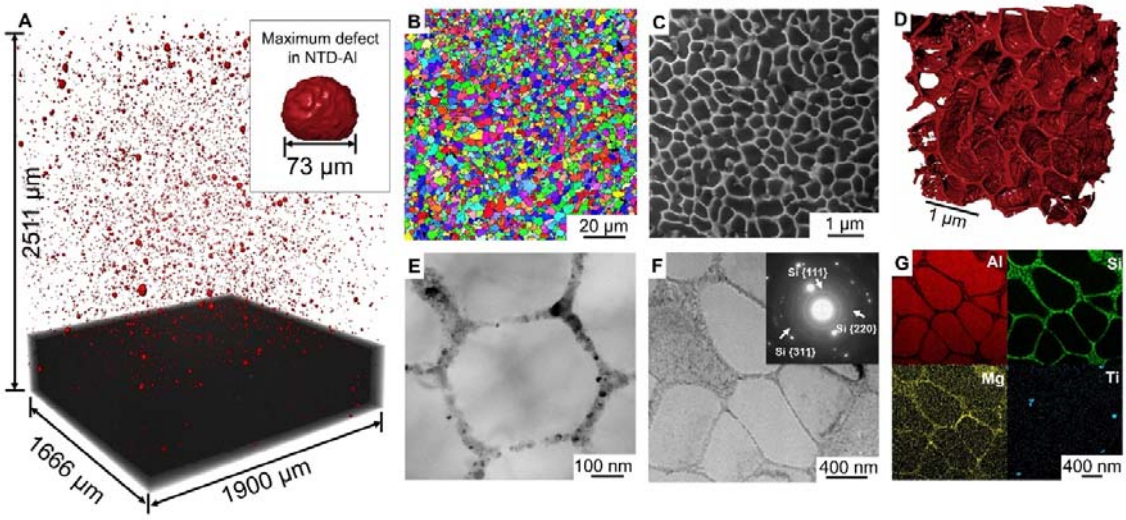


**Fig. 2 Microstructure of the AM NTD-Al alloy.** (A) μ-CT analysis showing the spatial and size distributions of printing defects, where the largest defect is measured to be 73 μm, only about 1/3 of the LOF defects in AM AlSi10Mg alloy without $TiB_2$ decoration (Extended Data Fig. 3A and B). (B) Grain morphology of the printed sample. (C) A network of solidification cellular structure with an average diameter of ~ 500 nm. (D) Continuous 3D Si cellular structure revealed by BSE/FIB tomography. (E) Cellular structure consisting of nanosized Si phases revealed by TEM. (F-G) TEM image and Al, Si, Mg and Ti EDS maps illustrating that the distribution of Si coinciding with the cellular structure. Inset showing the selected area electron diffraction (SAED) pattern illustrating Si existing as nanosized phases with random orientations.

Previous studies have demonstrated that the fatigue strength of conventional LPBF-AM AlSi10Mg is deteriorated by printing defects[6,24,25]. The printing defects induce stress concentration and thus are the key contributors to the inferior and scattered fatigue properties of metal AM parts compared to their wrought counterparts[6,24-26]. In order to rule out the complicated effects of printing defects and disclose the intrinsic fatigue strength limit related to the 3D-DPCN, *in situ* fatigue experiments were performed on micro-samples from pore-free areas. The 3D-DPCN, as a continuous integral network, is supposed to be the strongest obstacles to dislocation movements[27,28], compared to other structural characters such as

element solutions, precipitations, grain boundaries et.al, and thus determines the intrinsic fatigue behaviour. The size of the micro-samples fabricated using FIB was chosen to be gauge length of ~ 14 μm and cross section of ~ 4 × 4 $\mu m^2$, which contains around a thousand cellular nanostructures (Fig. 3A). Micro-tensile tests were first performed to find out the intrinsic mechanical response without the printing defects interference, where yield strength of ~ 470 MPa and ultimate tensile strength of ~ 550 MPa were measured (Extended data Fig. 5D, the *in-situ* movie available in Supplementary Video 1). The micro-tensile samples exhibited ductile behaviour with significant necking accompanied by gradual reduction of the cross-sectional area, as shown in Supplementary Video 1. The stress-strain curve was smooth without any strain burst or sudden load drop. It should be noticed that the dislocation slip bands[29] conventionally appeared during the *in situ* micro-test of metallic materials were not observed (Extended Data Fig. 5D), indicating that localised dislocation slips were suppressed. According to the tensile test results, two series of fatigue tests were conducted, one with maximum stress at the yielding stress, the other near the ultimate tensile stress, with sinusoidal cyclic loading tests at 100 Hz (Fig 3A, inset) and stress ratio of R = 0.1. Surprisingly, neither sign of damage accumulation (such as the persistent slip bands, PSBs) nor crack initiation could be observed on the sample surface after $10^7$ cycles loading at a maximum stress of 470 MPa (Fig. 3B, the *in situ* movie available in Supplementary Video 2). By contrast, when micro-sized Ni crystal was examined by a similar *in situ* fatigue test, slip band markings characteristic of PSB formation were observed[30]. The transmission Kikuchi diffraction (TKD) and local misorientation map of thin-section sample prepared from the fatigued area in Fig. 3C-E demonstrated that very limited residual strain was generated, indicating strain localisation was

totally restrained by the cell walls after long-term cyclic loading. These results suggest that the 3D-DPCN possesses an ultrahigh intrinsic fatigue strength limit above 470 MPa, which is more than doubled the highest fatigue strength limit of reported Al Alloys. The corresponding fatigue strength/tensile strength ratio is above 0.85, which has never been reported in any other metals to the best of our knowledge (Fig. 1B). When the maximum stress was raised to 520 MPa, detectable strain accumulation damage gradually developed in the form of necking during the course $10^5$ loading cycles (after which the test was stopped), while the intactness of the sample was still preserved (Fig. 3F and G, and see Supplementary Video 3). This result further proves that strain damage accumulation only generates in a reluctant manner at stress close to the tensile strength, which deserves future investigation. A same test was also conducted on LPBF-AM AlSi10Mg without $TiB_2$ decoration, where a fatigue strength limit ratio exceeding 0.85 was verified (Fig. S1 and see Supplementary Video 4), confirming that the intrinsic fatigue performance arises from the 3D-DPCN. These findings reveal a new route to the design of fatigue immunisation metals through additive manufacturing phase engineering.

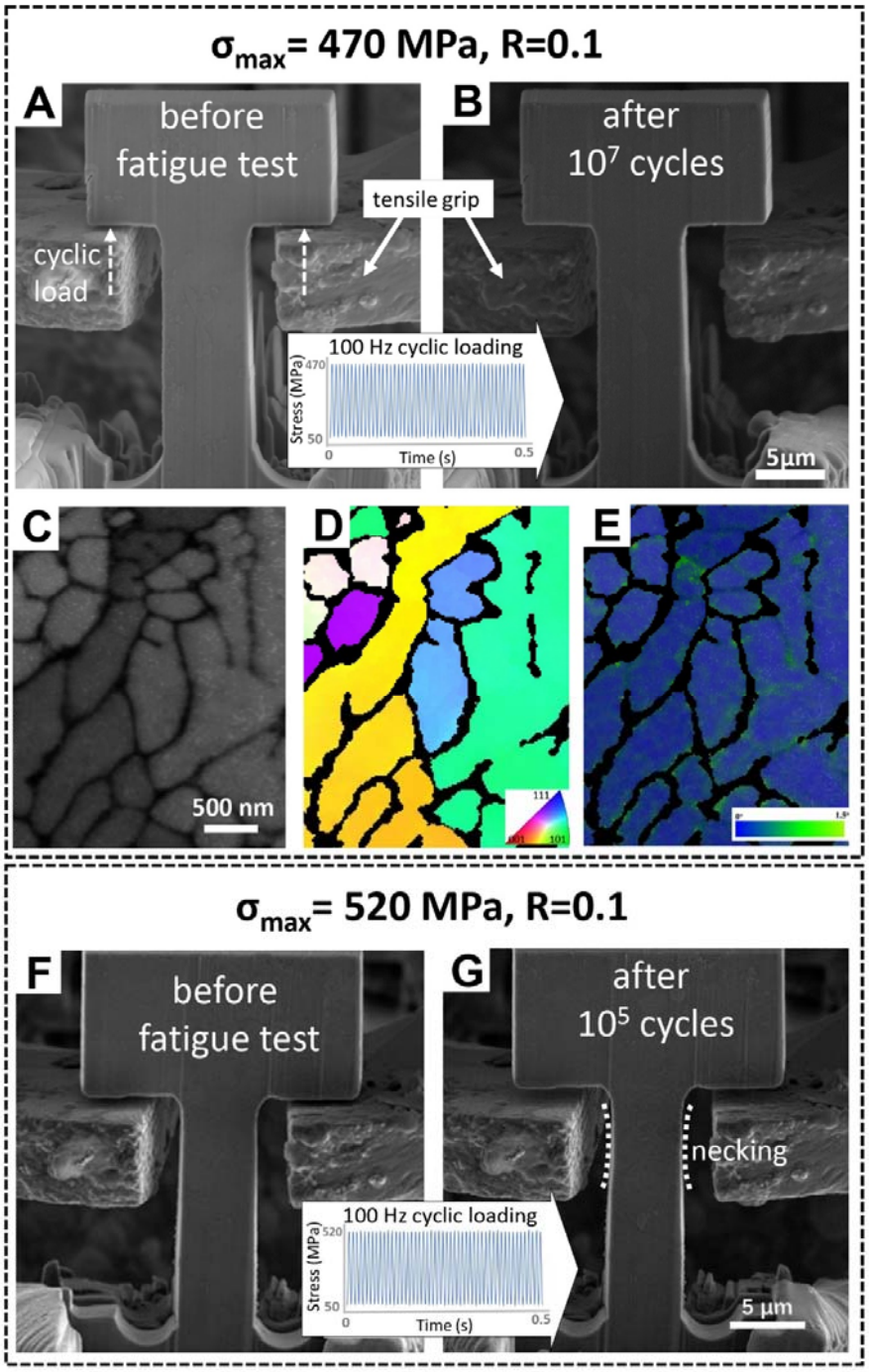


**Fig. 3 *In situ* micro-fatigue testing results**. SEM images of the micro-sample (A) before the fatigue test and (B) after $10^7$ loading cycles at the maximum stress of 470 MPa. Inset: loading curve showing 50 cycles in 0.5s (part of the total loading curve as an example) of stress from ~ 50 MPa to ~ 470 MPa. (C) Band contrast image of the sample after the fatigue test, with (D) TKD map and (E) local misorientation map. (F) SEM images of the micro-sample before the fatigue test and (G) after $10^5$ loading cycles at the maximum stress of 520 MPa. Inset: loading curve showing 50 cycles in 0.5s of stress from ~ 50 MPa to ~ 520 MPa.

To validate the functioning of the fatigue immunisation mechanism in bulk NTD-Al, fatigue tests with ASTM/ISO standard specimens (Extended Data Fig. 2) were performed on the as-printed NTD-Al alloy. Despite the relatively low ductility of approximately 6%–8% (Extended Data Fig. 6) and the abundance of printing defects (Fig. 2A), the fatigue strength limits of the NTD-Al alloy reached 260 MPa (pull-pull fatigue testing, stress ratio R = 0.1; printed by ProX DMP 200) and 250 MPa (rotary bending fatigue testing, stress ratio R = -1; printed by M280), which were more than double those of reported AM AlSi10Mg and high-strength AM AlMgScZr alloys (Fig. 1A)[5-9,14-22]. The rotary bending fatigue strength limit of 250 MPa (R = -1) even exceeded those of conventional 2XXX, 6XXX and 7XXX series wrought Al alloys (Fig. 1B)[2,10-13]. These findings indicate the vast potential applicability of our alloy for the lightweight structures necessary in industries, where the fatigue property is the key design criterion. Furthermore, the intrinsic fatigue strength limit of defect-free samples almost doubled the macro-fatigue strength, denoting that there is plenty space for further enhancement of fatigue resistance as shown in Fig. 1B.

The fatigue testing results illustrate that the fatigue strength limit of the ASTM standard NTD-Al samples almost doubled those of traditional AM AlSi10Mg alloys but was still half lower than that of the defect-free micro-size NTD-Al sample. Previous literature has shown that the fatigue strength limit of macro-size 3D printing samples is strongly associated with the largest printing defects[24,31]. μ-CT results showed that obvious LOF defects with irregular morphology were distributed throughout the AM AlSi10Mg alloys (Extended Data Fig. 3), while nearly spherical pores instead of LOF defects were uniformly distributed throughout the NTD-Al samples (Fig. 2A). Meanwhile, the size of the largest defect in AM NTD-Al alloys

was reduced to no more than one-third of that of the AM AlSi10Mg alloys (Extended Data Fig. 3). As the stress concentration from the defects is a crucial factor related to the fatigue resistance, the stress concentration factors of the largest defects drawn from the μ-CT results were estimated by the finite element method (FEM) in the AM NTD-Al and AM AlSi10Mg samples, respectively (Extended Data Fig. 7). The stress concentration factors of AM NTD-Al were generally between 2.2 and 3.0, while those of the irregular LOF defects in AM AlSi10Mg were 4.3 to 7.9. The greatly decreased pore sizes and the optimised porosity morphology are primarily responsible for the superior fatigue-resistance of AM NTD-Al compared with conventional AM AlSi10Mg.

We investigated the macro-specimens after $10^7$ fatigue cycles at a maximum stress of 260 MPa (R = 0.1) to assess the microstructural features after high cycle fatigue test. The fatigued area of the sample (2 mm × 2 mm × 6 mm in the middle of the specimen) was first characterised by μ-CT (Fig. 4A). Compared with the initial sample (Fig. 2A), no detectable changes in the defect characteristics were found, including the size, morphology and distribution of pores. Notably, no obvious cracks were observed in the characterised region after fatigue testing (Fig. 4A). However, as shown by the fracture surface of samples that failed at higher stress (Extended Data Fig. 8), the fatigue cracks usually initiate from the site of the largest defect near the surface of the sample, the size of which is in agreement with the μ-CT results. Therefore, two of the largest pores (P1 and P2) near the sample surface and two of the largest pores in the middle of the sample (P3 and P4) were selected for high-resolution μ-CT scanning of 0.5 μm voxel size. No cracks emerged from these pores as shown in the insets of Fig. 4A, confirming that the crack initiation was entirely suppressed even around the largest pores. In

order to reveal the fatigue immunisation mechanism of our macro samples, two TEM thin foils were lifted out from the fatigued areas using FIB to characterise the fatigued microstructure. One was from a randomly chosen area and the other was from the stress concentration area next to P1, which was located and exposed by μ-CT-guided laser polishing (Fig. 4B, details of the process can be found in Supplementary Information Fig. S2). The latter was lifted out at the edge of P1 on the plane parallel to the loading axis (Fig. 4C). Fig. 4D to F and Extended Data Fig. 9 showed that the Si cellular structure was not destroyed after fatigue loading. Even through the material at the edge of P1 was exposed to much larger cyclic loading due to the stress concentration effect, no notable changes were observed in the Si cellular structure (Fig. 4D). Under the applied stress of 260 MPa (fatigue limit of macro-sized sample), stress concentration of over 500 MPa estimated by FEM (Extended Data Fig. 7D) would be developed around the spherical pores, indicating that the critical stress of fatigue immunisation without damage accumulation is around 500 MPa, in agreement with our micro-fatigue test results (sample passed fatigue test at maximum stress of 470 MPa and damage accumulation manifested at maximum stress of 520 MPa, Fig. 3B and G).

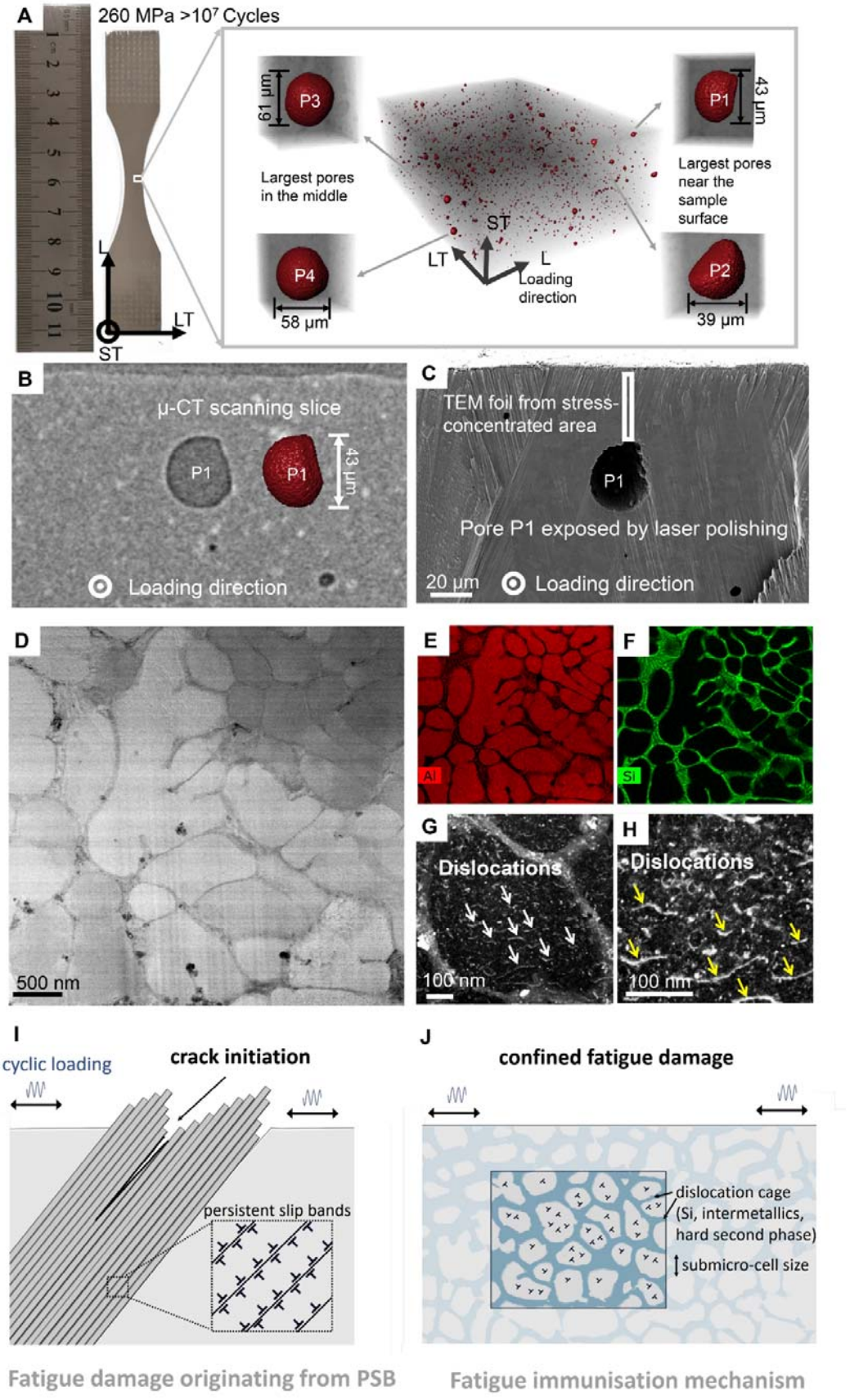


Fatigue damage originating from PSB

Fatigue immunisation mechanism

**Fig. 4 Fatigue mechanism investigation on the specimen after $10^7$ fatigue cycles at a maximum stress of 260 MPa (R = 0.1).** (A) No obvious cracks were observed in the specimen after fatigue testing; no cracks emerged from the largest pores (P1-P4); P1 and P2 were located close to the sample surface while P3 and P4 were in the middle of the sample. (B) μ-CT scanning cross-section of P1. (C) Locating and exposing the cross-section of P1 by μ-CT-guided laser polishing. (D) TEM characterisation of intact Si cellular structure in the region next to P1 (TEM foil lifted out from the rectangular region in Fig. 4C). (E-F) EDS maps illustrating the distribution Al and Si elements. (G-H) Individual dislocations distributed inside one Si nano-cellular structure. Schematics showing (I) the conventional fatigue damage originating from PSB and (J) the fatigue immunisation mechanism of 3D-DPCN structure.

The *in situ* fatigue test and the particular post-fatigue microstructure of the bulk sample prove a cyclic response totally immune to fatigue damage accumulation in our printed alloy. Based on the above analysis, we rationalised that the defects optimisation and 3D-DPCN were responsible for the high fatigue resistance of the LPBF-AM NTD-Al alloy. The 3D-DPCN hampers the conventional strain localisation associated with irreversible damage during fatigue loadings (Fig. 4I), such as persistent slip bands, veins, and dislocation cells, which were widely observed in various coarse-grained metals[32,33]. Instead, individual dislocations were observed inside the Si nano-cellular structure (Fig. 4G and H). This coincides with the results observed in copper film that as the grain reduced to below 1 μm, the generation of dislocation substructures was inhibited and only individual dislocations were formed after fatigue test[34]. Similar microstructural fatigue features have also been observed in other ultrafine-grain alloys[35], where the limited space for dislocation movement inhibits the formation of fatigue dislocation patterns, resulting in increased resistance to crack initiation and high fatigue resistance. For instance, an ultrafine-grained high-entropy alloy has been found to exhibit a high fatigue ratio of approximately 0.62 times its ultimate tensile strength[36]. Besides, A recent *in situ* TEM compression test on AM AlSi10Mg showed that during deformation, the dislocations generated were constrained inside the cells, where no obvious penetration through

the cell boundaries was observed[28]. These results provide microstructural evidence confirming that the 3D nano-cellular Si phase of approximately 500 nm in size acts as a strong volumetric 3D dislocation barrier nanocage that traps dislocation movement inside during fatigue load. By this manner, long-range dislocation slips and dislocation reorganisation were strongly inhibited during fatigue loading, thereby preventing the formation of strain localisation fatigue damage (Fig. 4J). Thus, a fatigue strength limit close to its tensile strength can be guaranteed without fatigue damage accumulation and crack initiation.

The 3D-DPCN shows a characteristic fatigue response with no shearing or damage accumulation below the critical stress, which has significant advantages in industry compared with conventional alloys where the unpredictability of fatigue damage accumulation raises great uncertainty. Based on our work a paradigm of achieving high fatigue resistance through additive manufacturing phase engineering has been established from nanoscale microstructural design to the fabrication of geometrically intricate industrial components. Utilizing *in situ* micro-scale tests, the intrinsic fatigue strength limits of the 3D-DPCN can be measured, the results of which could be incorporated with defects distribution from the CT analysis and stress distribution from the simulation of industrial components, so that the fatigue response of an AM component can be predicted to assist performance-oriented processing optimisation. One such example of meter-scale engine blade design is given in Fig. 1C and D.

In this work, we reported a defect-optimised bulk AM NTD-Al alloy that has a record high fatigue strength that greatly surpassed that of previously reported AM Al alloys and conventional high-strength wrought Al alloys obtained by different thermal-mechanical processes. A novel fatigue immunisation mechanism was revealed in Al-alloys prepared by

LPBF-AM, where the inherent 3D-DPCN network resulted from the rapid solidification is able to confine fatigue damage via acting as a strong volumetric 3D dislocation barrier cage to prevent the localised irreversible damage accumulation during fatigue cyclic loading. Further enhancement of the fatigue resistance of NTD-Al is expected by decreasing the printing defect size to the sub-micron range or by eliminating defects through future technological innovations. Our anti-fatigue paradigm has also been validated in industry scale components, including aircraft door hinges and engine blades. Furthermore, this fatigue damage immunisation mechanism enabled by additive manufacturing phase engineering approach could also be extended to the design of other fatigue-resistant dual/multi-phase alloy systems (another example is given in supplemental materials) and to other additive manufacturing techniques including electron beam melting and directed energy deposition.

## Methods

### Powder fabrication

The nano-$TiB_2$-decorated AlSi10Mg powder was fabricated by an *in situ* salt-metal reaction method and gas atomisation[14]. Extended Data Fig. 1 shows the spherical morphology of our *in situ* synthesised powders, which ensures a much better flowability. The flowability of our powders was measured to be ~ 20 s/50 g through Hall flowmeter measurement. It can be observed from the magnified image of the cross section of powder that the *in situ* synthesised $TiB_2$ nanoparticles are homogeneously distributed in the powder (Extended Data Fig. 1B and C).

Previous works shows that $TiB_2$ particles can ameliorate the laser printing process through (a) increasing the average laser energy density[14]; (b) modifying the solidification path by promote grain nucleation and mitigate solidification defects[23,37-39]; and (c) stabilizing melt pool fluctuations and preventing liquid droplet coalesce, which result in the elimination of large spatters and the reduction of printing defects[23,40]. As shown in Extended Data Fig. 1E and F, the laser reflectivity of Al-Si-Mg alloy can be reduced by ~ 40% with 5% addition of $TiB_2$, while the K-M absorption factor was raised by ~ 220%. With the addition of $TiB_2$ particles, the detrimental LOF defects have been eliminated (Fig. 2A and Extended Data Fig.3). The chemical composition is shown in Extended Data Table 1.

### Laser powder bed fusion additive manufacturing

LPBF additive manufacturing of NTD-Al samples for standard fatigue test was performed using 3D Systems Prox DMP 200 and EOS M280 selective laser melting machines. The fan blades of aircraft engine were manufactured by a customised BLT-S500 selective laser melting

machine. An inert, high-purity (≥99.99%) argon gas atmosphere flow with an oxygen content of < 600 ppm was used throughout the process to minimise oxidation. The AM processing was completed at room temperature without applying heat to the build plate. The printing parameters used in our work were listed in Extended Data Table 1. The samples consisted of 3 mm × 21 mm × 105 mm and 12 mm × 28 mm × 130 mm blocks for the fatigue tests; 5 mm × 5 mm blocks for microstructure characterisation; and 2 mm × 10 mm × 60 mm blocks for the tensile tests. Images of the as-printed samples are shown in Extended Data Fig. 2.

**Sectioning and sample preparation**

As-printed samples were removed from the build plates by wire electrical discharge machining. The fatigue samples were polished using 400, 800, 1200 and 2500 grit sandpaper consecutively and then with 5 μm diamond suspensions, which ensured a deformation-free surface. The scanning electron microscopy (SEM) and EBSD samples were polished with 400, 800, 1200 and 2500 grit sandpaper. Final polishing of these samples was conducted with the diamond suspensions, followed by ion polishing in a Leica EM TIC 3X. Some of the polished samples were etched using Keller's etchant to reveal the 3D cellular Si structure (Fig. 2C).

The TEM and TKD lamellas were prepared in a Tescan Lyra3 FIB/SEM microscope. A protective platinum layer was deposited at 30 kV and a current of 200 pA. FIB trenches were roughly milled under 30 kV and 10 nA. Cross-sections were finely polished using a 3 nA current. After lifting out the sample and welding it to a Cu TEM grid, the lamellas were thinned under 30 kV, with the current reduced in the sequence of 1 nA, 500 pA, 150 pA and 50 pA. Final polishing was conducted at 5 kV and a 50 pA current.

**Microstructure and defect characterisation**

The microstructures of the as-fabricated alloys were characterised with a SEM (Tescan Lyra3) equipped with EBSD (Oxford Nordlys Max3). The EBSD maps were recorded with step size of 0.1 μm. The orientation evolution of the fatigued samples was characterised using TKD with step size of 30 nm (Oxford Nordlys Max3). TEM (FEI Tecnai G2 operating at 200 kV) was used to examine the Si cellular structure.

**Reconstruction of printing defects**

X-ray μ-CT was performed using Xradia 510 Versa (Zeiss) to analyse the printing defects inside the SLM-printed samples. A voxel size of 3.0 μm was selected to allow the large specimen volumes (up to 2 mm × 2 mm × 6 mm) to be imaged. High-resolution μ-CT scanning (0.5 μm voxel size) was further performed on localised regions. Reconstruction of the scanned volumes was conducted using Dragonfly software. The defect population was resolved with respect to the position and volume.

**Reconstruction of 3D dual-phase cellular nanostructure**

To obtain 3D volumes of the studied materials, SEM was coupled with the FIB milling technique (Lyra3 Tescan). The angle between the FIB and SEM columns was 55°. Before running the acquisition, a Pt layer (10 ×10 ×1 μm) was deposited on an area of interest by ion beam deposition (IBD) to smooth out the surface roughness and protect the target surface. A micropillar (10 ×10 × 20 μm) was prepared for the 3D acquisition. After acquiring an BSE image at the side surface of the micropillar, a 15 nm step of material was removed using FIB. Serial FIB sectioning was done with a current of 1 nA at 5 keV. The following BSE 2D image was acquired and this process was repeated several hundred times to obtain an 3D volume with

a resolution of 15 nm. The collected 2D images of the elemental-Si contrast were reconstructed by Dragonfly software.

**Tensile and Fatigue test**

Dog-bone tensile testing specimens were machined according to the ASTM-E8M standard. The tests were carried out on a Zwick/Roell Z100 testing machine at a constant strain rate of $10^{-4}$ $s^{-1}$.

Fatigue testing specimens were machined according to the ASTM E466-21 standard for pull-pull fatigue test, R = 0.1 (Extended Data Fig. 2C) and the ISO 1143-2008 for rotating bending fatigue test, R = -1 (Extended Data Fig. 2D), respectively. High-frequency fatigue testing machines were used for the rotating bending fatigue test (R = -1) (Giga Quad YRB200; Yamamoto Corporation, Japan) and the pull-pull fatigue test (R = 0.1) (Changchun Qianbang Corporation, China). The cyclic loading followed a sinusoidal wave. A frequency of 80 Hz was used for both fatigue tests. The tests were conducted in air at room temperature (approximately 21 °C and 30% relative humidity). The high cycle fatigue tests were terminated after $10^7$ cycles, with the surviving samples being identified as run-outs.

**Micro-sample fabrication**

For the *in situ* micro-tests, "T"-shaped micro-specimen geometry was fabricated as shown in Extended Data Fig. 5. The gauge regions were rectangular in cross-section with approximate dimensions of 4 × 4 $\mu m^2$, while the gauge lengths were approximately 14 μm. The "T" head region was approximately 15 μm in width and the same thickness as the gauge section. During the test, the "T" head would be lifted from the underneath at two sides to induce tensile load at

the gauge region. Chamfering was introduced at the two ends of the gauge region to reduce local stress concentration.

The micro-specimens were fabricated at the top edge of the printed sample after mechanical surface polishing, so that the top and front views of micro-specimen could be exposed to laser and ion milling. The first step of fabrication was rough-milling the geometry using a Gemini2 (Zeiss) femtosecond laser operated at 4.5 W with a repetition rate of 1.0 kHz. After laser milling, FIB in Tescan Lyra3 SEM-FIB was used to obtained the final gauge geometry. Surface imperfections and curtaining, as well as tapering of the specimen, were minimised by performing a low-current final polishing step at 30 kV, 150 pA.

**Micro-testing methodology**

The micro-tensile and fatigue tests were performed utilizing an Alemnis Standard Assemble platform inside of a Tescan Lyra3 SEM. A customised diamond tensile grip was used to induce tensile load to the specimen (Extended Data Fig. 5A and B). During the FIB polishing of "T"-shape geometry, several adjustments was made to ensure full contact between the "T"-head and the tensile grip at the two sides, so that the tensile load will be applied along the gauge axis.

For the tensile test, a nominal strain rate of $10^{-3}$ $s^{-1}$ was applied using the displacement-controlled mode. For the fatigue test, the cyclic loading was introduced through applying sinusoidal displacement signal at 100 Hz. The stress level was controlled by adjusting the input displacement value and amplitude to perform the R=0.1 fatigue test. The load and displacement data were tracked and recorded at 1kHz frequency. The displacement signal was recalibrated after each $10^4$ loading cycles (100 s) to minimise the effect of mechanical drifting.

## References and Notes


1 Suresh, S. *Fatigue of Materials*. 2 edn, (Cambridge University Press, 1998).

2 Zhang, Q., Zhu, Y., Gao, X., Wu, Y. & Hutchinson, C. Training high-strength aluminum alloys to withstand fatigue. *Nature Communications* **11**, 5198, doi:10.1038/s41467-020-19071-7 (2020).

3 Koyama, M. *et al.* Bone-like crack resistance in hierarchical metastable nanolaminate steels. *Science* **355**, 1055, doi:10.1126/science.aal2766 (2017).

4 Pan, Q., Zhou, H., Lu, Q., Gao, H. & Lu, L. History-independent cyclic response of nanotwinned metals. *Nature* **551**, 214-217, doi:10.1038/nature24266 (2017).

5 Tang, M. & Pistorius, P. C. Oxides, porosity and fatigue performance of AlSi10Mg parts produced by selective laser melting. *International Journal of Fatigue* **94**, 192-201, doi: 10.1016/j.ijfatigue.2016.06.002 (2017).

6 Ch, S. R., Raja, A., Jayaganthan, R., Vasa, N. J. & Raghunandan, M. Study on the fatigue behaviour of selective laser melted AlSi10Mg alloy. *Materials Science and Engineering: A* **781**, 139180, doi:https://doi.org/10.1016/j.msea.2020.139180 (2020).

7 Brandl, E., Heckenberger, U., Holzinger, V. & Buchbinder, D. Additive manufactured AlSi10Mg samples using Selective Laser Melting (SLM): Microstructure, high cycle fatigue, and fracture behavior. *Materials & Design* **34**, 159-169, doi:https://doi.org/10.1016/j.matdes.2011.07.067 (2012).

8 Aboulkhair, N. T., Maskery, I., Tuck, C., Ashcroft, I. & Everitt, N. M. Improving the fatigue behaviour of a selectively laser melted aluminium alloy: Influence of heat treatment and surface quality. *Materials & Design* **104**, 174-182, doi:https://doi.org/10.1016/j.matdes.2016.05.041 (2016).

9 He, P. *et al.* Fatigue and dynamic aging behavior of a high strength Al-5024 alloy fabricated by laser powder bed fusion additive manufacturing. *Acta Materialia* **220**, 117312, doi:https://doi.org/10.1016/j.actamat.2021.117312 (2021).

10 Committee, A. I. H. *Volume 02 - Properties and Selection: Nonferrous Alloys and Special-Purpose Materials*. (ASM International, 1990).

11 Committee, A. I. H. *Volume 19 - Fatigue and Fracture*. (ASM International, 1996).

12 Henry, S. D. *et al. Fatigue Data Book - Light Structural Alloys*. (ASM International, 1995).

13 Kaufman, J. G. *Properties of Aluminum Alloys - Fatigue Data and the Effects of Temperature, Product Form, and Processing*. (ASM International, 2008).

14 Mower, T. M. & Long, M. J. Mechanical behavior of additive manufactured, powder-bed laser-fused materials. *Materials Science and Engineering: A* **651**, 198-213, doi:10.1016/j.msea.2015.10.068 (2016).

15 Mishra, R. S. & Thapliyal, S. Design approaches for printability-performance synergy in Al alloys for laser-powder bed additive manufacturing. *Materials & Design* **204**, doi:10.1016/j.matdes.2021.109640 (2021).

16 Uzan, N. E., Ramati, S., Shneck, R., Frage, N. & Yeheskel, O. On the effect of shot-peening on fatigue resistance of AlSi10Mg specimens fabricated by additive manufacturing using selective laser melting (AM-SLM). *Additive Manufacturing* **21**, 458-464, doi:10.1016/j.addma.2018.03.030 (2018).

17 Damon, J., Dietrich, S., Vollert, F., Gibmeier, J. & Schulze, V. Process dependent porosity and the influence of shot peening on porosity morphology regarding selective laser melted AlSi10Mg parts. *Additive Manufacturing* **20**, 77-89, doi:10.1016/j.addma.2018.01.001 (2018).

18 Bassoli, E., Denti, L., Comin, A., Sola, A. & Tognoli, E. Fatigue Behavior of As-Built L-PBF A357.0 Parts. *Metals* **8**, doi:10.3390/met8080634 (2018).

19 Uzan, N. E., Shneck, R., Yeheskel, O. & Frage, N. Fatigue of AlSi10Mg specimens fabricated by additive manufacturing selective laser melting (AM-SLM). *Materials Science and Engineering: A* **704**, 229-237, doi:10.1016/j.msea.2017.08.027 (2017).

20 Siddique, S., Awd, M., Tenkamp, J. & Walther, F. High and very high cycle fatigue failure mechanisms in selective laser melted aluminum alloys. *Journal of Materials Research* **32**, 4296-4304, doi:10.1557/jmr.2017.314 (2017).

21 Awd, M. *et al.* Comparison of Microstructure and Mechanical Properties of Scalmalloy((R)) Produced by Selective Laser Melting and Laser Metal Deposition. *Materials (Basel)* **11**, doi:10.3390/ma11010017 (2017).

22 Suryawanshi, J. *et al.* Simultaneous enhancements of strength and toughness in an Al-12Si alloy synthesized using selective laser melting. *Acta Materialia* **115**, 285-294, doi:10.1016/j.actamat.2016.06.009 (2016).

23 Li, X. P. *et al.* Selective laser melting of nano-TiB2 decorated AlSi10Mg alloy with high fracture strength and ductility. *Acta Materialia* **129**, 183-193, doi:10.1016/j.actamat.2017.02.062 (2017).

24 Sanaei, N. & Fatemi, A. Defects in additive manufactured metals and their effect on fatigue performance: A state-of-the-art review. *Progress in Materials Science* **117**, 100724, doi:https://doi.org/10.1016/j.pmatsci.2020.100724 (2021).

25 Romano, S., Abel, A., Gumpinger, J., Brandão, A. D. & Beretta, S. Quality control of AlSi10Mg produced by SLM: Metallography versus CT scans for critical defect size assessment. *Additive Manufacturing* **28**, 394-405, doi:10.1016/j.addma.2019.05.017 (2019).

26 Haridas, R. S., Thapliyal, S., Agrawal, P. & Mishra, R. S. Defect-based probabilistic fatigue life estimation model for an additively manufactured aluminum alloy. *Materials Science and Engineering: A* **798**, doi:10.1016/j.msea.2020.140082 (2020).

27 Zhang, X. X. *et al.* Evolution of microscopic strains, stresses, and dislocation density during in-situ tensile loading of additively manufactured AlSi10Mg alloy. *International Journal of Plasticity* **139**, doi:10.1016/j.ijplas.2021.102946 (2021).

28 Wu, J., Wang, X. Q., Wang, W., Attallah, M. M. & Loretto, M. H. Microstructure and strength of selectively laser melted AlSi10Mg. *Acta Materialia* **117**, 311-320, doi:https://doi.org/10.1016/j.actamat.2016.07.012 (2016).

29 Reichardt, A. *et al.* In situ micro tensile testing of He+2 ion irradiated and implanted single crystal nickel film. *Acta Materialia* **100**, 147-154, doi:https://doi.org/10.1016/j.actamat.2015.08.028 (2015).

30 Lavenstein, S., Gu, Y., Madisetti, D. & El-Awady, J. A. The heterogeneity of persistent slip band nucleation and evolution in metals at the micrometer scale. *Science* **370**, doi:10.1126/science.abb2690 (2020).

31 Wu, Z. *et al.* The effect of defect population on the anisotropic fatigue resistance of AlSi10Mg alloy fabricated by laser powder bed fusion. *International Journal of Fatigue* **151**, 106317, doi:https://doi.org/10.1016/j.ijfatigue.2021.106317 (2021).

32 Li, P., Li, S. X., Wang, Z. G. & Zhang, Z. F. Unified factor controlling the dislocation evolution of fatigued face-centered cubic crystals. *Acta Materialia* **129**, 98-111, doi:https://doi.org/10.1016/j.actamat.2017.02.057 (2017).

33 Pineau, A., McDowell, D. L., Busso, E. P. & Antolovich, S. D. Failure of metals II: Fatigue. *Acta Materialia* **107**, 484-507, doi:https://doi.org/10.1016/j.actamat.2015.05.050 (2016).

34 Zhang, G. P. *et al.* Length-scale-controlled fatigue mechanisms in thin copper films. *Acta Materialia* **54**, 3127-3139, doi:https://doi.org/10.1016/j.actamat.2006.03.013 (2006).

35 Vinogradov, A. & Hashimoto, S. Multiscale Phenomena in Fatigue of Ultra-Fine Grain Materials-an Overview. *Materials Transactions* **42**, 74-84 (2001).

36 Liu, K., Nene, S. S., Frank, M., Sinha, S. & Mishra, R. S. Extremely high fatigue resistance in an ultrafine grained high entropy alloy. *Applied Materials Today* **15**, 525-530, doi:10.1016/j.apmt.2019.04.001 (2019).

37 Prasad, A. *et al.* Towards understanding grain nucleation under Additive Manufacturing solidification conditions. *Acta Materialia* **195**, 392-403, doi:https://doi.org/10.1016/j.actamat.2020.05.012 (2020).

38 Fan, Z. *et al.* Grain refining mechanism in the Al/Al–Ti–B system. *Acta Materialia* **84**, 292-304, doi:https://doi.org/10.1016/j.actamat.2014.10.055 (2015).

39 StJohn, D. H., Qian, M., Easton, M. A. & Cao, P. The Interdependence Theory: The relationship between grain formation and nucleant selection. *Acta Materialia* **59**, 4907-4921, doi:https://doi.org/10.1016/j.actamat.2011.04.035 (2011).

40 Qu, M. *et al.* Controlling process instability for defect lean metal additive manufacturing. *Nature Communications* **13**, 1079, doi:10.1038/s41467-022-28649-2 (2022).

**Acknowledgments:** We acknowledge L.A. Jiao and X.J. Cao from Carl Zeiss (Shanghai) for their aid in micro-CT analysis and micro-CT-guided laser polishing experiment, as well as W. Li from Tescan China for his support on FIB-SEM experiments.

**Funding:**

National Natural Science Foundation of China grant 51971137 (ZC)

National Natural Science Foundation of China grant 52101043 (CD)

National Natural Science Foundation of China grant 52101179 (JL)

Conseil Regional du Nord-Pas de Calais (GJ)

European Regional Development Fund (ERDF, GJ)

**Author contributions:**

Conceptualisation: ZC, JL

Methodology: YW, CD, HW, HL, MW, QS, SM, LW

Investigation: CD, YC, YW, HC, GJ, YX, AA, JL

Visualisation: CD, YL, HC, YZ, HL,

Funding acquisition: ZC, CD, GJ, HW

Project administration: ZC, CD, YW

Supervision: ZC, JL

Writing – original draft: ZC, CD

Writing – review & editing: ZC, JL, CD, YC

**Competing interests:** Authors declare that they have no competing interests.

**Data and materials availability:** All data are available in the main text or the supplementary materials. The data generated during and/or analysed during the current study are available from the corresponding author. Correspondence and requests for materials should be addressed to Zhe Chen.

# Extended data for

## Achieving Ultrahigh Fatigue-Resistant Al Alloys by Additive Manufacturing

Chengyi Dan[1,2]†, Yuchi Cui[1]†, Yi Wu[2]†, Zhe Chen[1,2]†*, Hui Liu[3], Gang Ji[4], Yakai Xiao[2], Han Chen[2], Mingliang Wang[1], Jun Liu[2], Lei Wang[2], Yang Li[2], Ahmed Addad[4], Ying Zhou[2], Siming Ma[2], Qiwei Shi[2], Haowei Wang[1,2], Jian Lu[3]*

Correspondence to: zhe.chen@sjtu.edu.cn, jianlu@cityu.edu.hk.

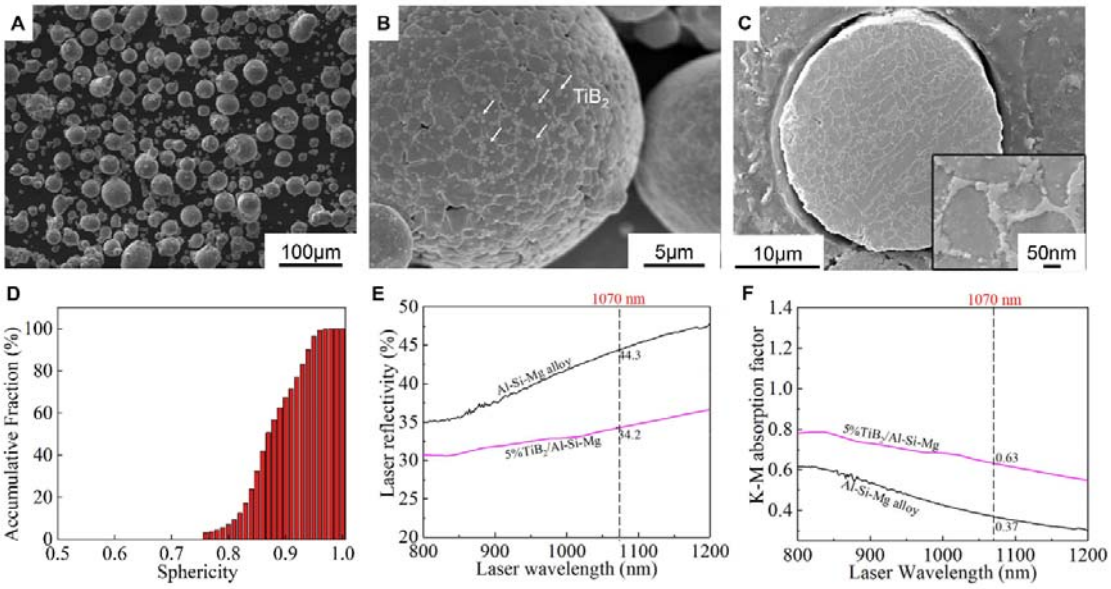


**Extended Data Fig. 1 AlSi10Mg powders decorated with $TiB_2$ nanoparticles.** (A-B) $TiB_2$/AlSi10Mg powders with spherical morphology. (C) Cross-section of powder showing the homogeneously distributed Si cells and $TiB_2$ particles. (D) Statistic analysis of the sphericity of $TiB_2$/AlSi10Mg powders. The laser reflectivity (E) and K-M absorption factor (F) of the AlSi10Mg and 5% $TiB_2$/AlSi10Mg powders. The laser absorption rate of 5% $TiB_2$/AlSi10Mg powders have been significantly increased by introducing nano-$TiB_2$ particles.

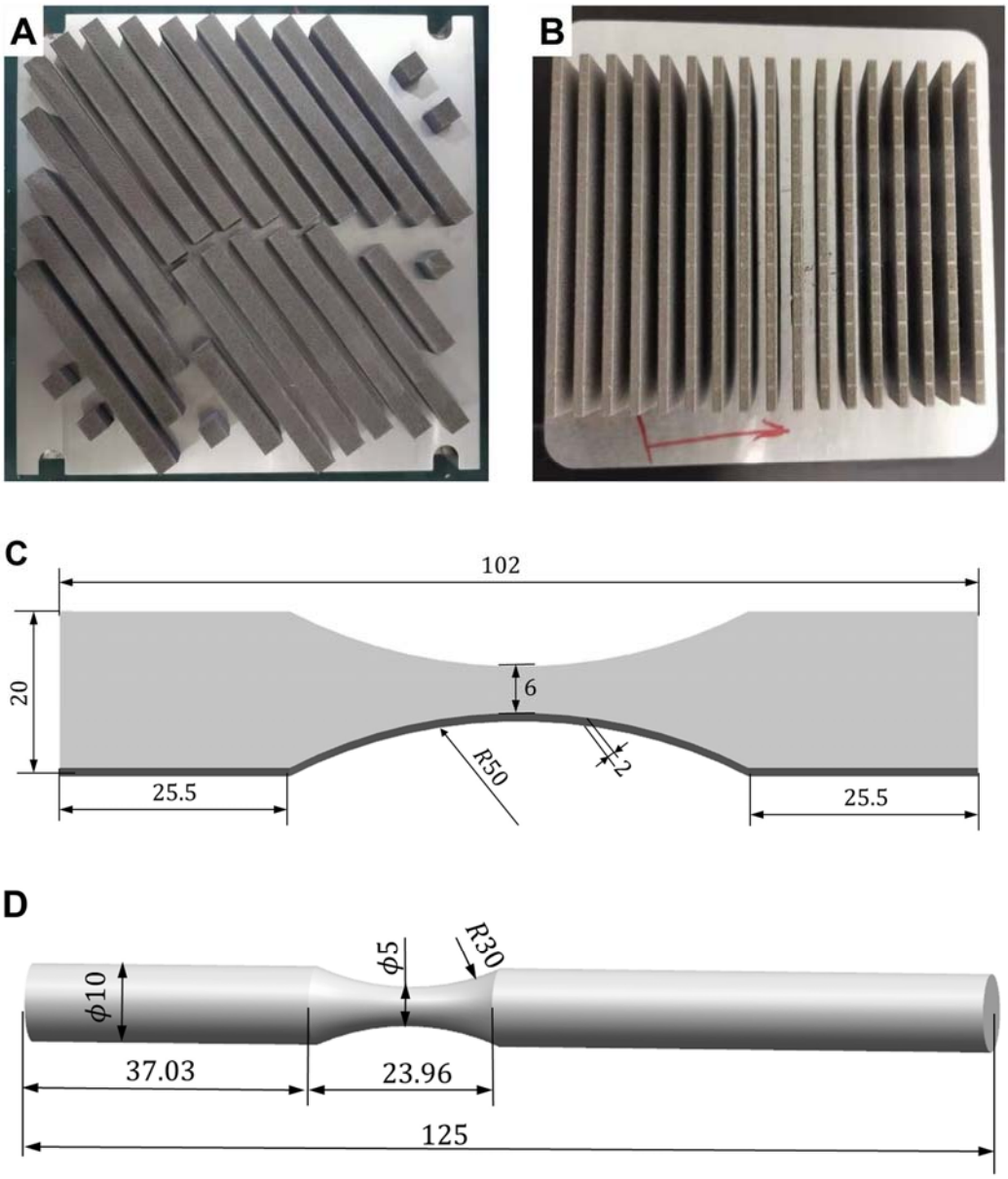


561

562 **Extended Data Fig. 2 As-printed NTD-Al alloy fatigue testing specimens.** (A) Samples
563 constructed by machine EOS M280. (B) Samples constructed by machine 3D Systems ProX
564 MP 200. **Schematics of fatigue testing specimen dimensions.** (C) Pull-pull fatigue test

565 sample geometry in mm, R = 0.1 (ASTM E466-21). (D) Rotating bending fatigue test sample

566 geometry in mm, R = -1 (ISO 1143-2008).

567

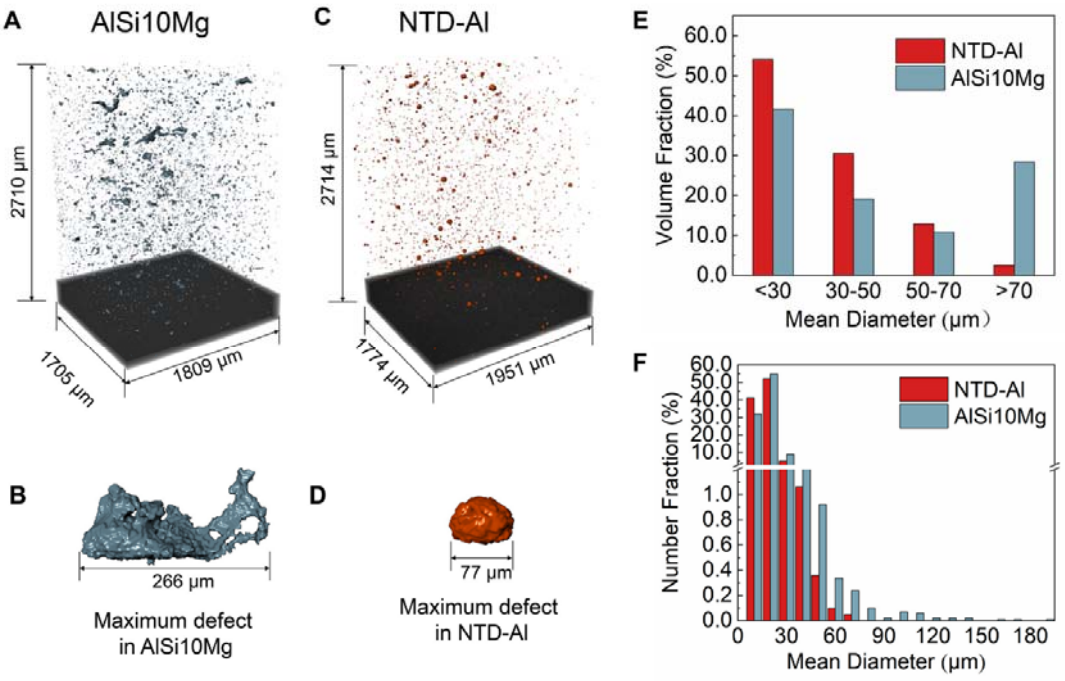


568

569 **Extended Data Fig. 3 μ-CT analysis showing the spatial and size distributions of defects.**

570 (A) Defects with irregular morphology in AM AlSi10Mg alloy. (B) The maximum defect in

571 the AlSi10Mg sample with the length about 266 μm. (C) Defects with near spherical

572 morphology in AM NTD-Al alloy manufactured by EOS M280. (D) The maximum defect in

573 the NTD-Al sample with the diameter about 77 μm. (E-F) Comparison of number and volume

574 fractions of defects in different size ranges.

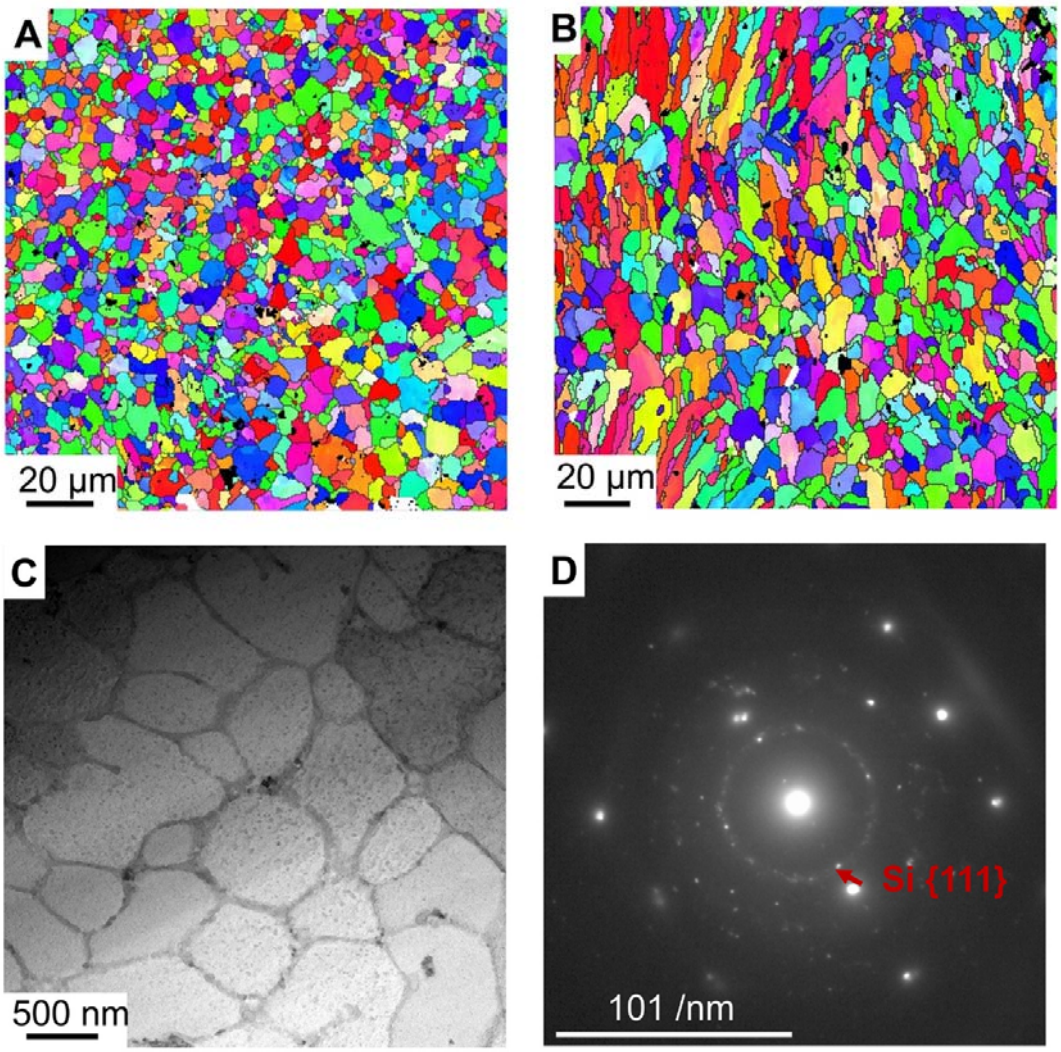


**Extended Data Fig. 4 Microstructure characterisation of the NTD-Al sample manufactured by EOS M280.** (A) Grain morphology of the plane perpendicular to the printing direction. (B) Grain morphology of the plane parallel to the printing direction. (C) Network of solidification cellular structure with an average diameter of ~ 500 nm. (D) Selected-area electron diffraction pattern indicating that Si existed as nanosized phases with random orientations.

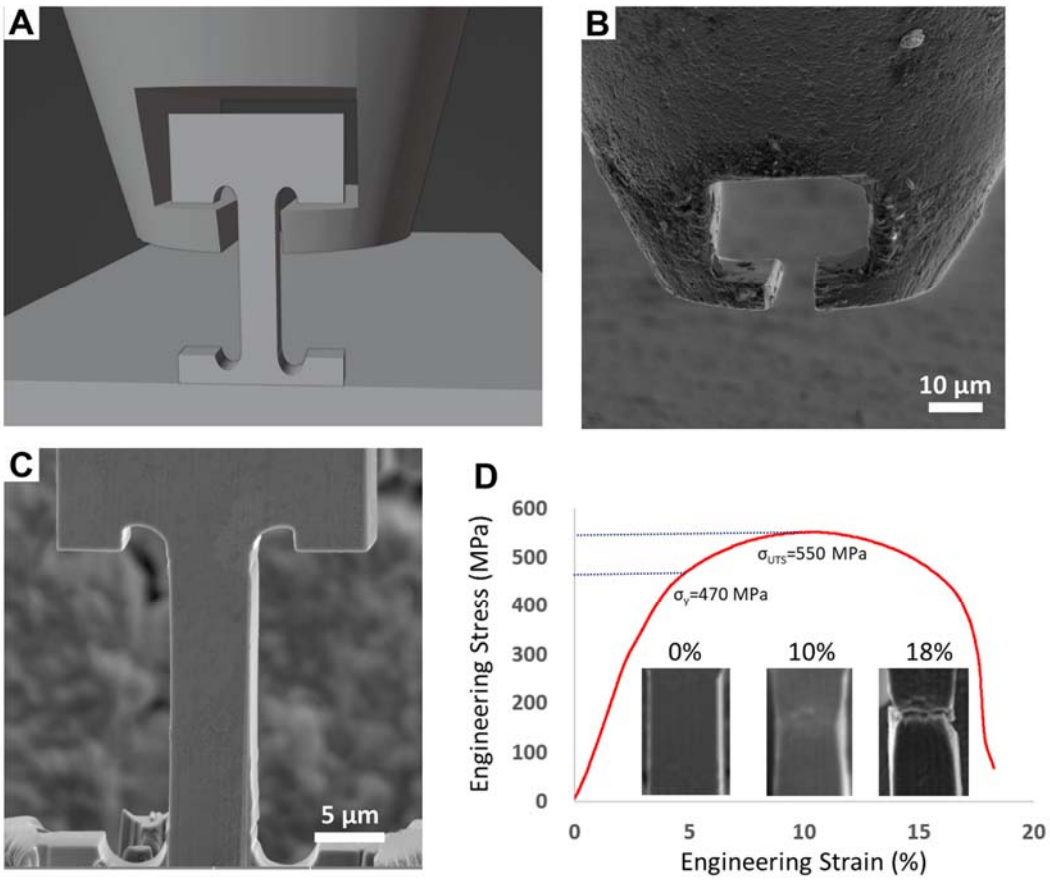


582

583 **Extended Data Fig. 5 *In situ* micro-mechanical testing.** (A) Geometry of the tensile grip
584 and micro-specimen. SEM images of (B) the customised diamond tensile grip and (C) the
585 micro-specimen. (D) Stress-strain curve measured from the *in situ* micro-tensile test, inset:
586 SEM images of the necked region at different strain levels.

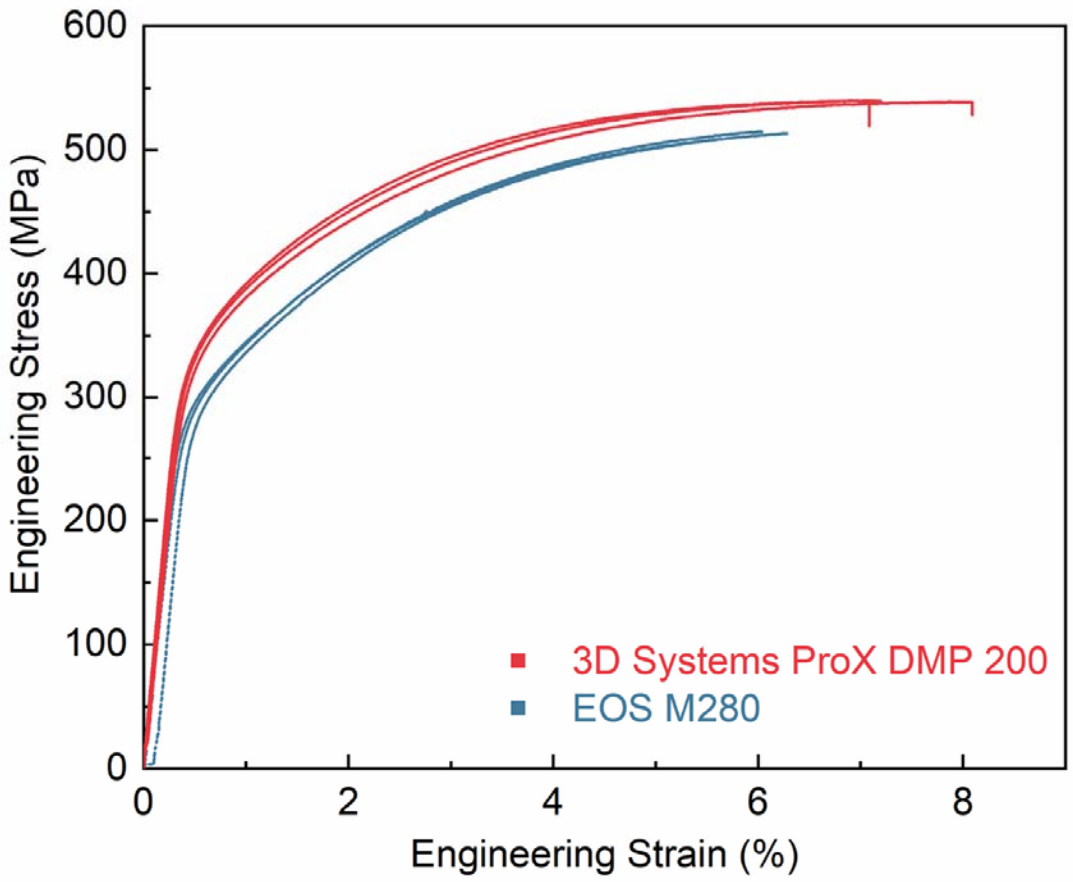


587

588 **Extended Data Fig. 6 Tensile Properties of as-printed NTD-Al.** Engineering stress–strain

589 curves of as-printed NTD-Al alloys by the two additive manufacturing machines.

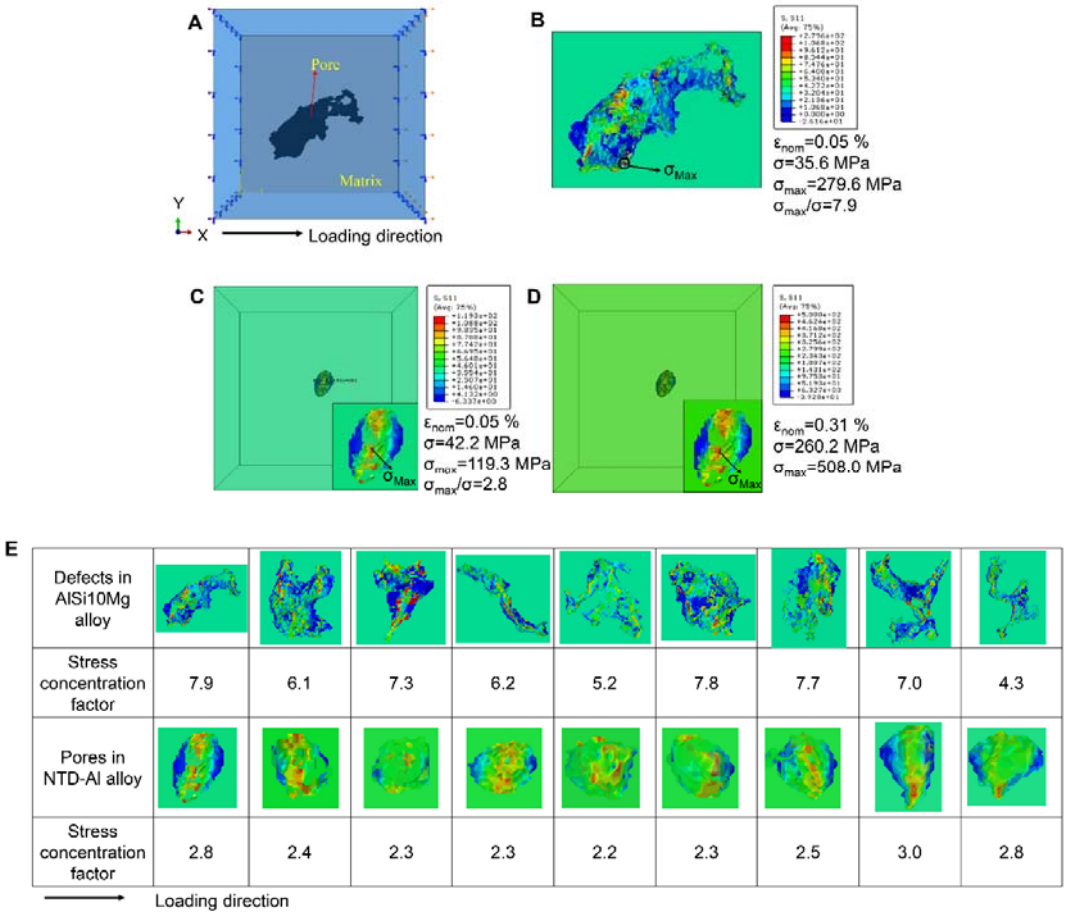


590

591 **Extended Data Fig. 7 FEM simulation of the stress concentration caused by the internal**

592 **pores in the AMAlSi10Mg alloy and AM NTD-Al alloy.** (A) An example of the FEM model

593 with an irregular LOF defect inside the AM AlSi10Mg alloy matrix. (B) Stress distribution

594 near the typical LOF defect surface in the AM AlSi10Mg alloy under a nominal strain of 0.05%.

595 (C) Stress distribution of a typical spherical pore in the AM NTD-Al alloy under a nominal

596 strain of 0.05%. (D) Stress distribution of the typical spherical pore under a nominal strain of

597 0.31% when the stress of the matrix is close to the fatigue strength (~ 260 MPa). € Stress

598 concentration factors of nine large irregular LOF defects in the AM AlSi10Mg sample and nine

599 typical pores in the AM NTD-Al sample.

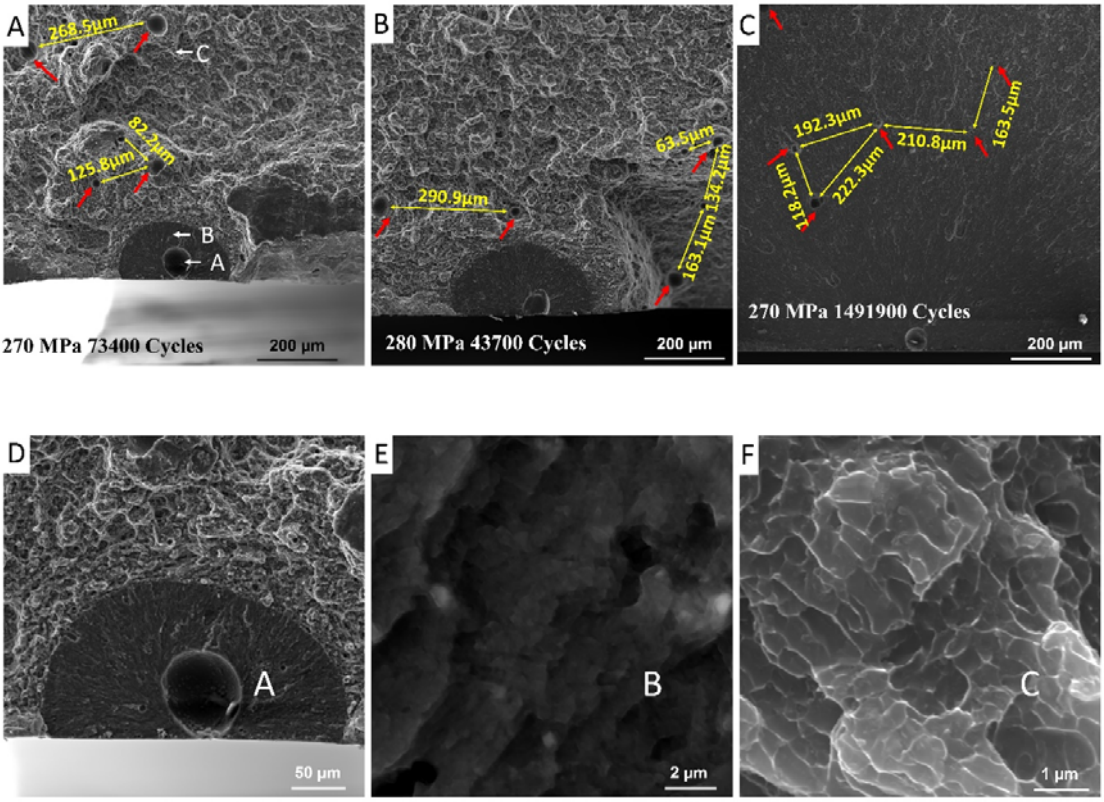


600

601 **Extended Data Fig. 8 Fractographic observations of fatigue failures in AM NTD-Al alloy.** (A-C) Fracture

602 surface of AM NTD-Al alloy at different fatigue loading strength, R=0.1; (D-F) three typical regions pointed out

603 by white arrows in Extended Fig. 8A. The fatigue crack usually initiates at the largest pore next to the sample

604 surface. Many smaller defects were also found on the fracture surface. The interspacing between neighboring

605 defects ranges from tens to hundreds of microns. Obvious Si cellular boundaries were also found on the fracture

606 surface.

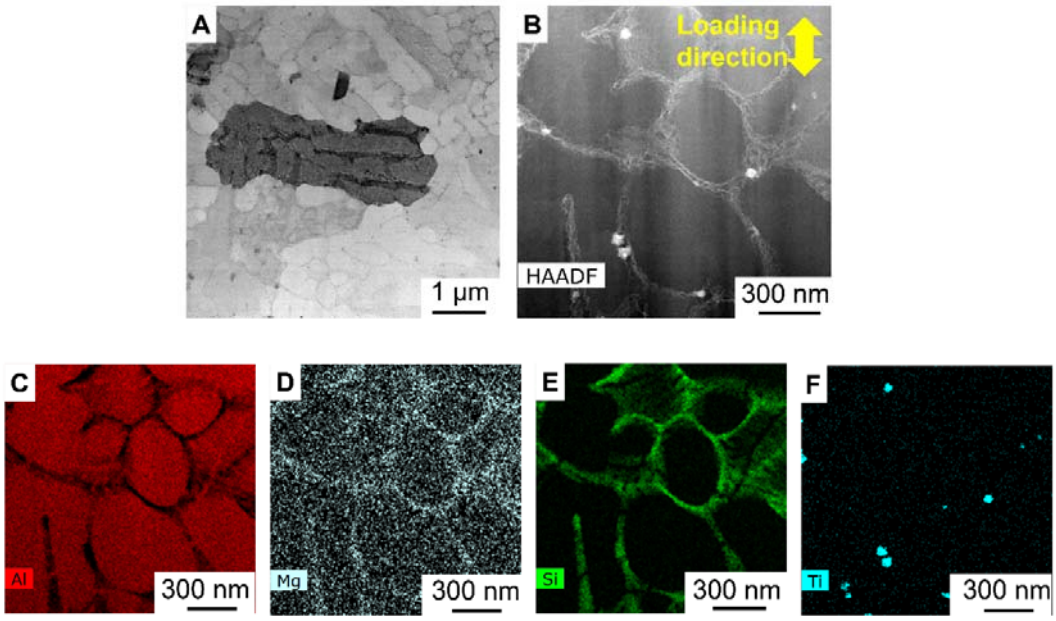


607

608 **Extended Data Fig. 9 Si cellular structure of the AM NTD-Al alloys after $10^7$ fatigue**

609 **testing cycles at a maximum stress of 260 MPa (R = 0.1).** (A-B) HAADF STEM images

610 showing the intact Si cellular structure. TEM samples were prepared from randomly selected

611 area from the gauge section of the sample after fatigue testing. (C-F) EDS maps illustrating the

612 distribution Al, Si, Mg and Ti elements.

613

**Extended Data Table 1 Chemical composition (wt.%) and additive manufacturing processing parameters of NTD-Al and AlSi10Mg powders (**The corresponding weight and volume fractions of the $TiB_2$ nanoparticles were ~ 5 wt.% and ~ 3.4 vol.%, respectively)

| Element | Si | Mg | Cu | Mn | Ti | B | Al |
|---|---|---|---|---|---|---|---|
| NTD-Al | 9.8 | 0.32 | <0.03 | <0.01 | 3.84 | 1.76 | Balance |
| AlSi10Mg | 10.1 | 0.32 | <0.03 | <0.01 | / | / | Balance |

| Parameter | | Laser power (W) | Laser diameter (μm) | Scanning speed (mm/s) | Layer thickness (μm） | Rotation angle (°) | Hatching space (μm） |
|---|---|---|---|---|---|---|---|
| AlSi10Mg | ProX DMP 200 | 280 | 75 | 1000 | 30 | 66.7° | 100 |
| NTD-Al | ProX DMP 200 | 280 | 75 | 1200 | 30 | 66.7° | 100 |
| NTD-Al | EOS M280 | 320 | 75 | 1000 | 30 | 66.7° | 100 |

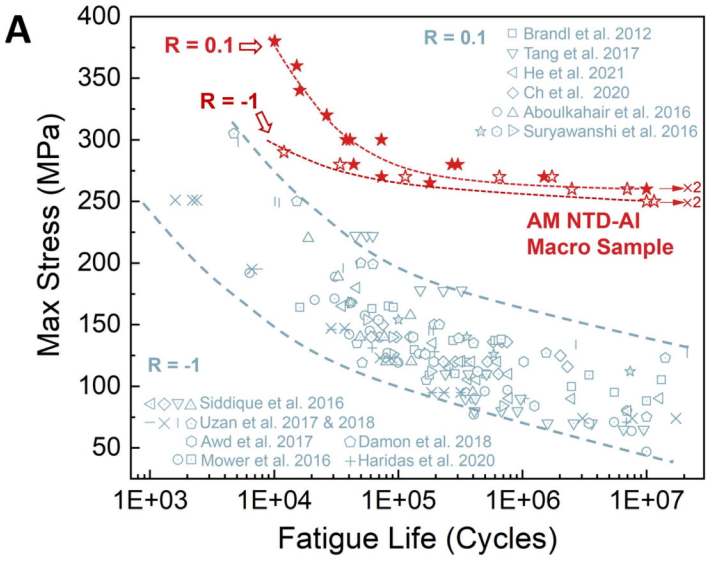
A
R = 0.1
R = -1
R = 0.1
Brandl et al. 2012
Tang et al. 2017
He et al. 2021
Ch et al. 2020
Aboulkahair et al. 2016
Suryawanshi et al. 2016
AM NTD-Al
Macro Sample
R = -1
Siddique et al. 2016
Uzan et al. 2017 & 2018
Awd et al. 2017
Damon et al. 2018
Mower et al. 2016
Haridas et al. 2020
Max Stress (MPa)
Fatigue Life (Cycles)

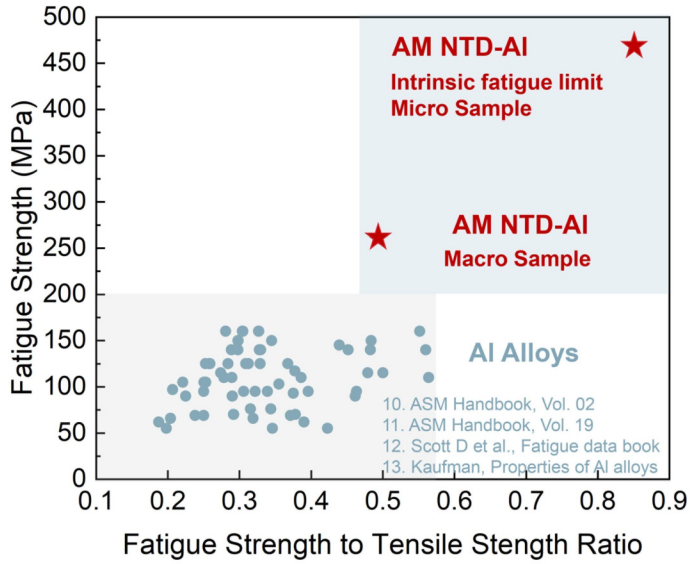
B
AM NTD-Al
Intrinsic fatigue limit
Micro Sample
AM NTD-Al
Macro Sample
Al Alloys
10. ASM Handbook, Vol. 02
11. ASM Handbook, Vol. 19
12. Scott D et al., Fatigue data book
13. Kaufman, Properties of Al alloys
Fatigue Strength (MPa)
Fatigue Strength to Tensile Stength Ratio

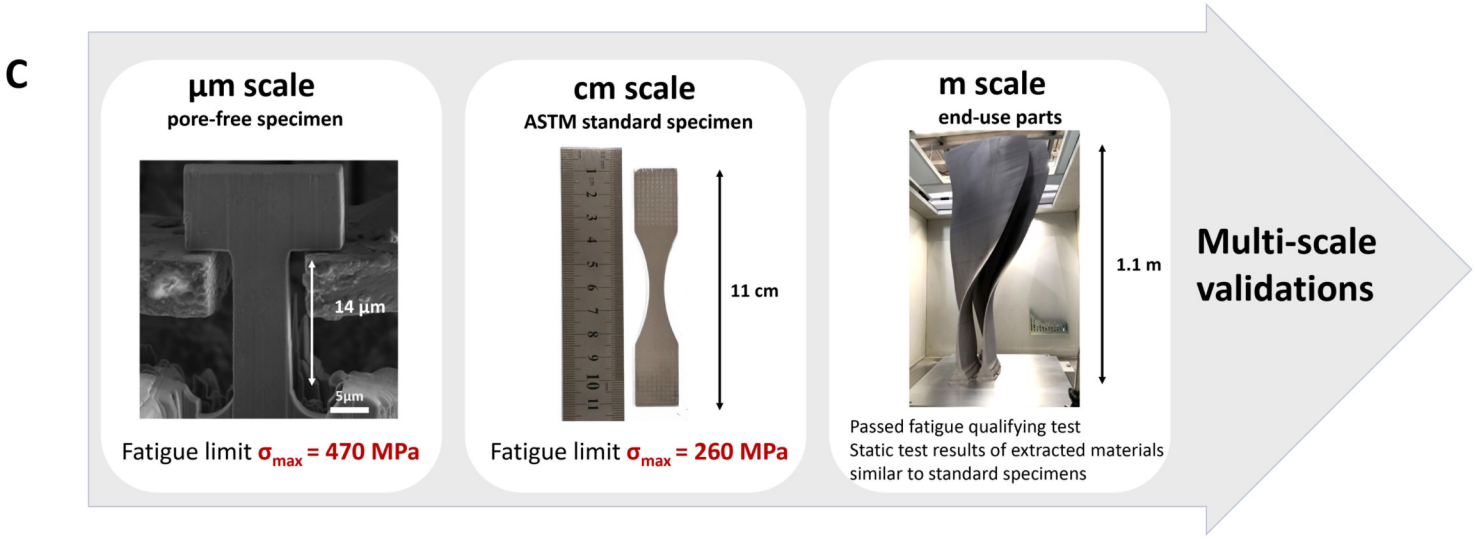
C
µm scale
pore-free specimen
14 µm
5µm
Fatigue limit σmax = 470 MPa
cm scale
ASTM standard specimen
11 cm
Fatigue limit σmax = 260 MPa
m scale
end-use parts
1.1 m
Passed fatigue qualifying test
Static test results of extracted materials
similar to standard specimens
Multi-scale
validations

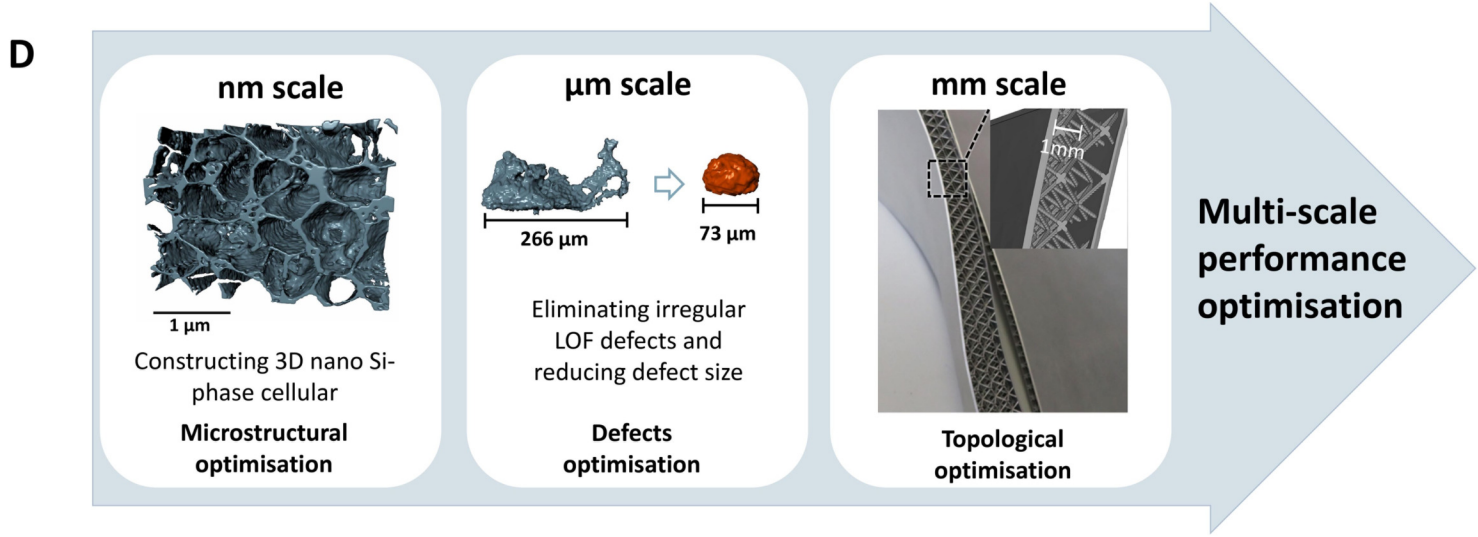
D
nm scale
1 µm
Constructing 3D nano Si-
phase cellular
Microstructural
optimisation
µm scale
266 µm
73 µm
Eliminating irregular
LOF defects and
reducing defect size
Defects
optimisation
mm scale
1mm
Topological
optimisation
Multi-scale
performance
optimisation

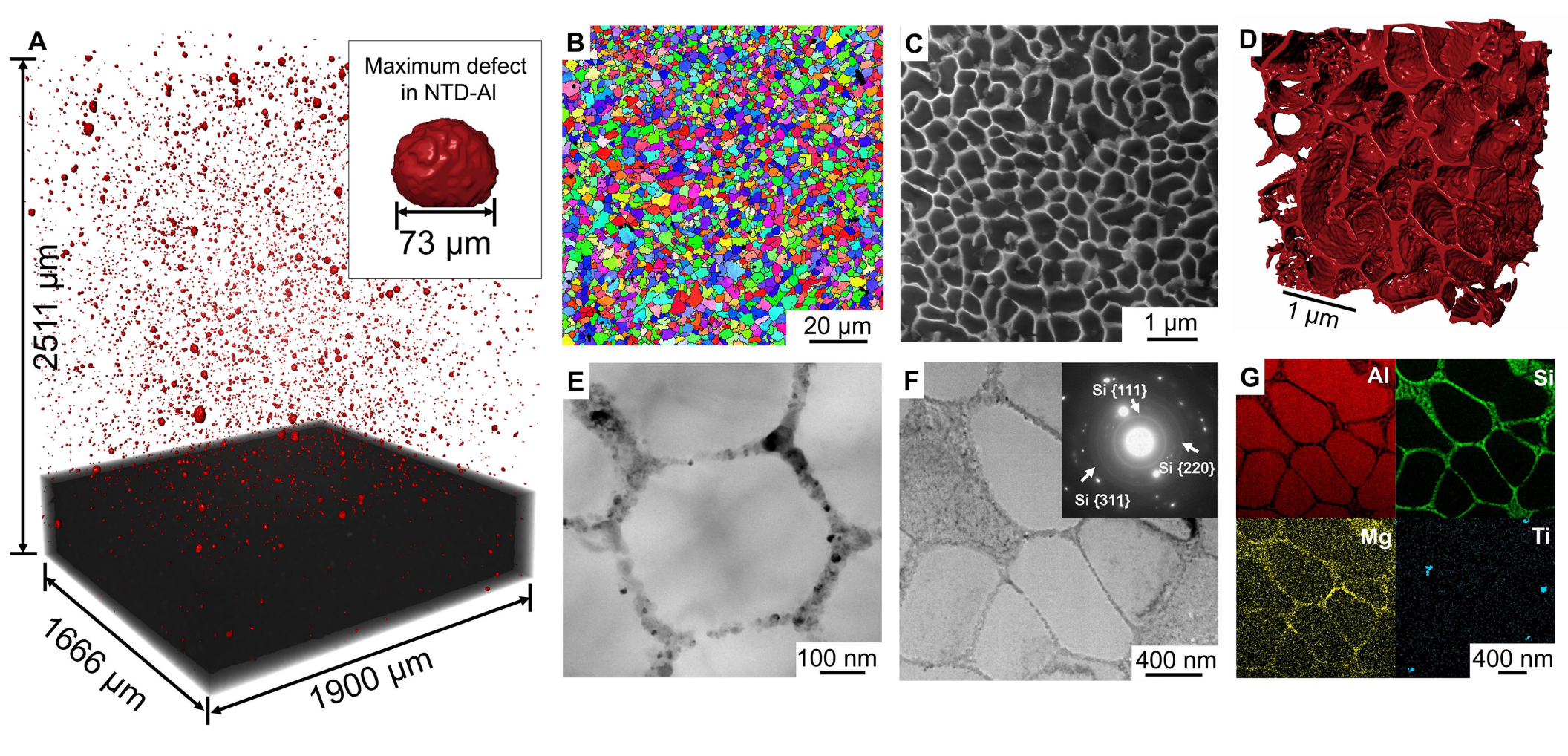
A
Maximum defect in NTD-Al
73 μm
2511 μm
1666 μm
1900 μm
B
20 μm
C
1 μm
D
1 μm
E
100 nm
F
Si {111}
Si {220}
Si {311}
400 nm
G
Al
Si
Mg
Ti
400 nm

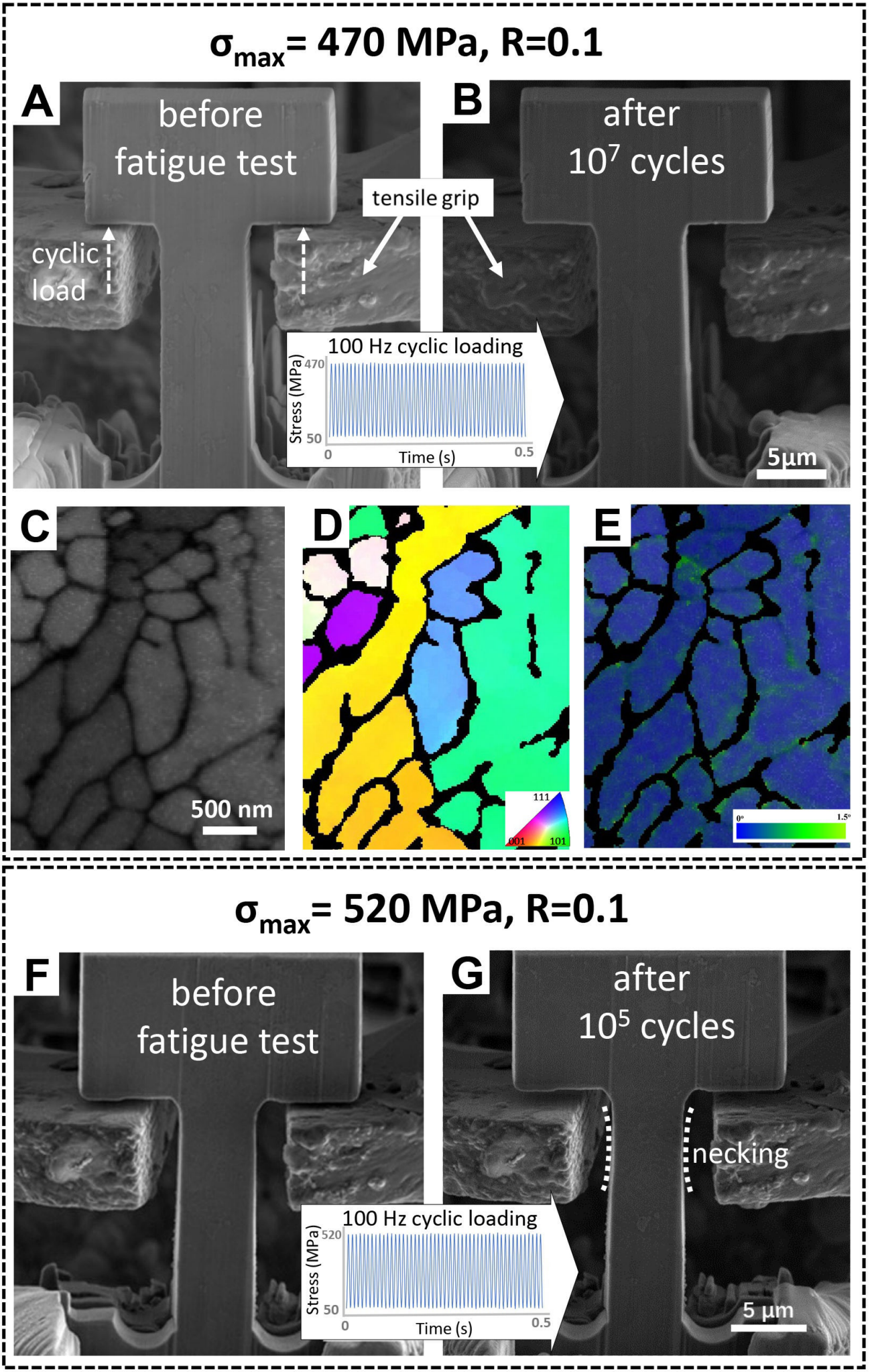
σmax= 470 MPa, R=0.1
A
before fatigue test
B
after 10^7 cycles
tensile grip
cyclic load
100 Hz cyclic loading
Stress (MPa)
470
50
0
Time (s)
0.5
5µm
C
500 nm
D
111
001
101
E
0°
1.5°
σmax= 520 MPa, R=0.1
F
before fatigue test
G
after 10^5 cycles
necking
100 Hz cyclic loading
Stress (MPa)
520
50
0
Time (s)
0.5
5 µm

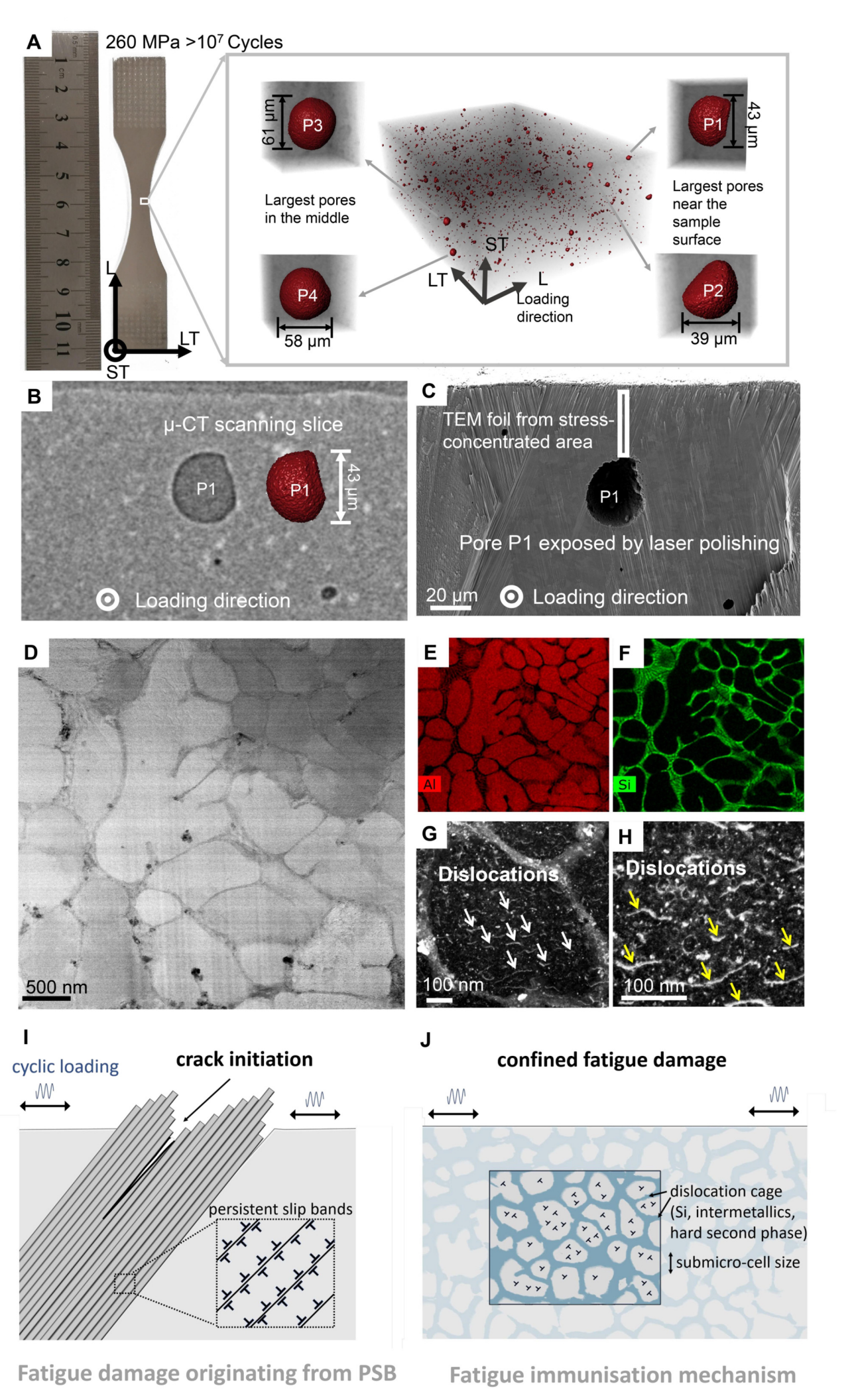
A
260 MPa >10⁷ Cycles
L
LT
ST
P3
61 μm
Largest pores in the middle
P1
43 μm
Largest pores near the sample surface
ST
LT
L
Loading direction
P4
58 μm
P2
39 μm
B
μ-CT scanning slice
P1
P1
43 μm
Loading direction
C
TEM foil from stress-concentrated area
P1
Pore P1 exposed by laser polishing
20 μm
Loading direction
D
500 nm
E
Al
F
Si
G
Dislocations
100 nm
H
Dislocations
100 nm
I
cyclic loading
crack initiation
persistent slip bands
J
confined fatigue damage
dislocation cage
(Si, intermetallics, hard second phase)
submicro-cell size
Fatigue damage originating from PSB
Fatigue immunisation mechanism

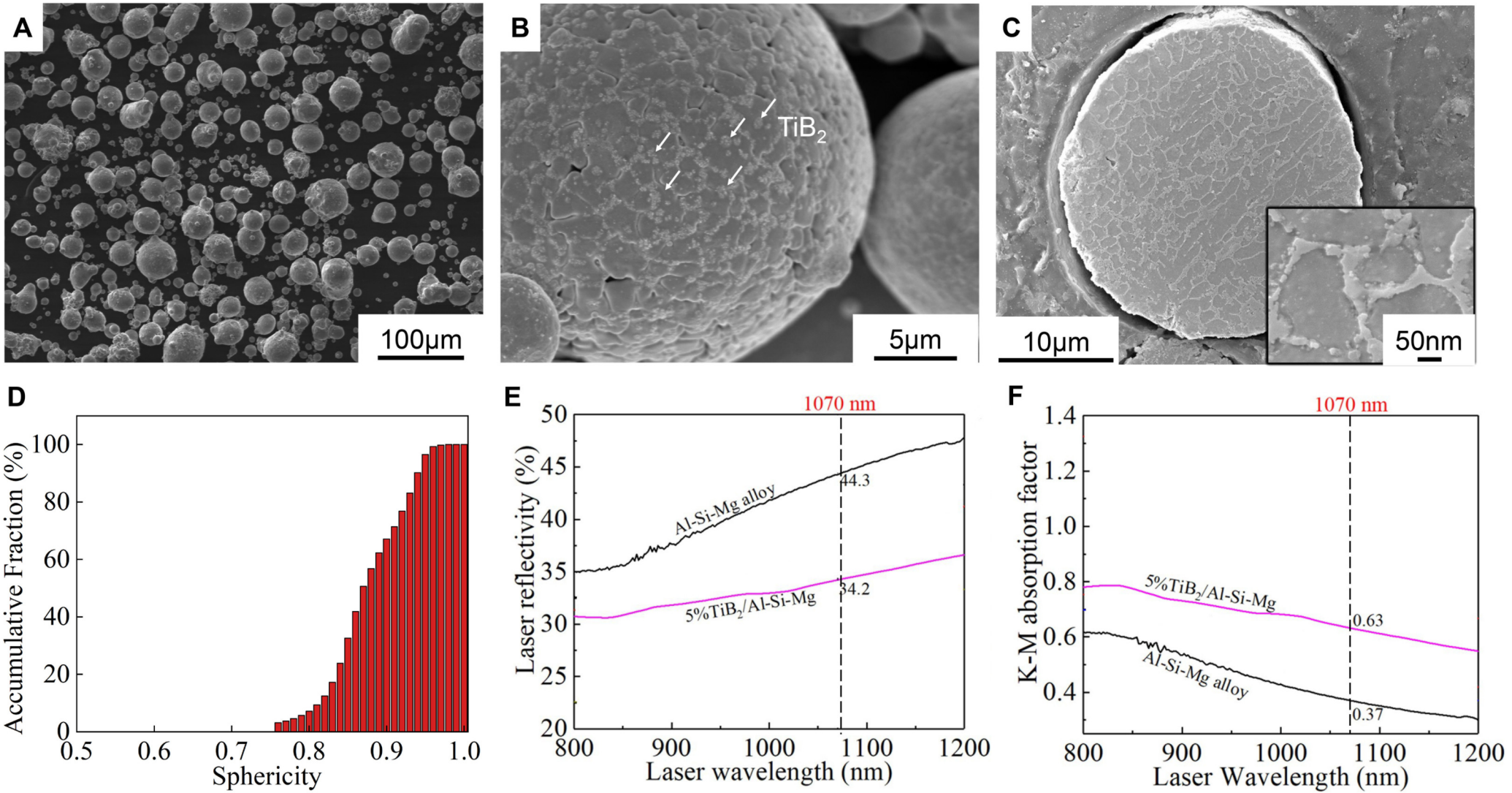
A
100μm
B
TiB2
5μm
C
10μm
50nm
D
Accumulative Fraction (%)
Sphericity
E
1070 nm
Laser reflectivity (%)
Al-Si-Mg alloy
5%TiB2/Al-Si-Mg
44.3
34.2
Laser wavelength (nm)
F
1070 nm
K-M absorption factor
5%TiB2/Al-Si-Mg
Al-Si-Mg alloy
0.63
0.37
Laser Wavelength (nm)

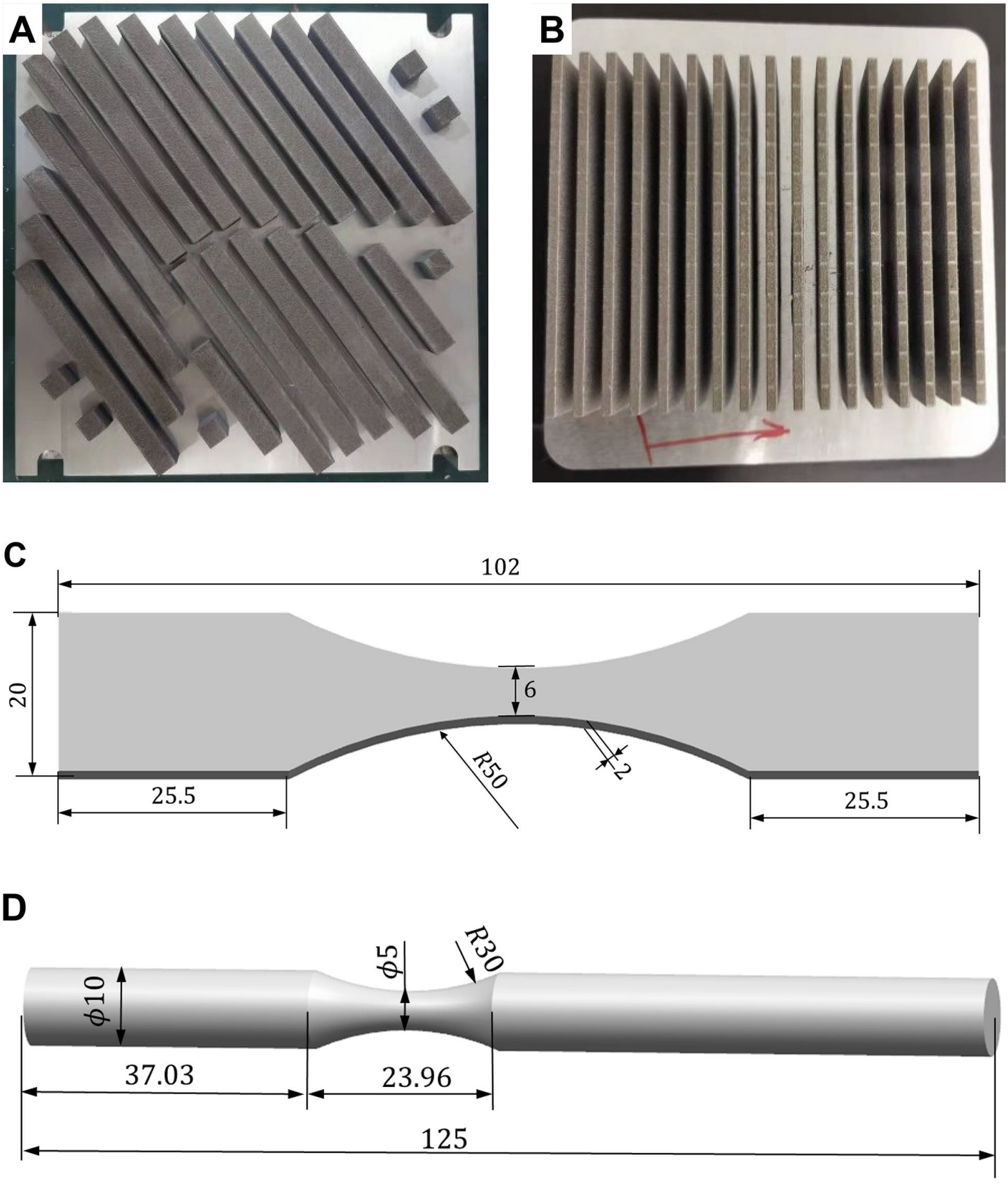
A
B
C
102
20
6
R50
2
25.5
25.5
D
ϕ10
ϕ5
R30
37.03
23.96
125

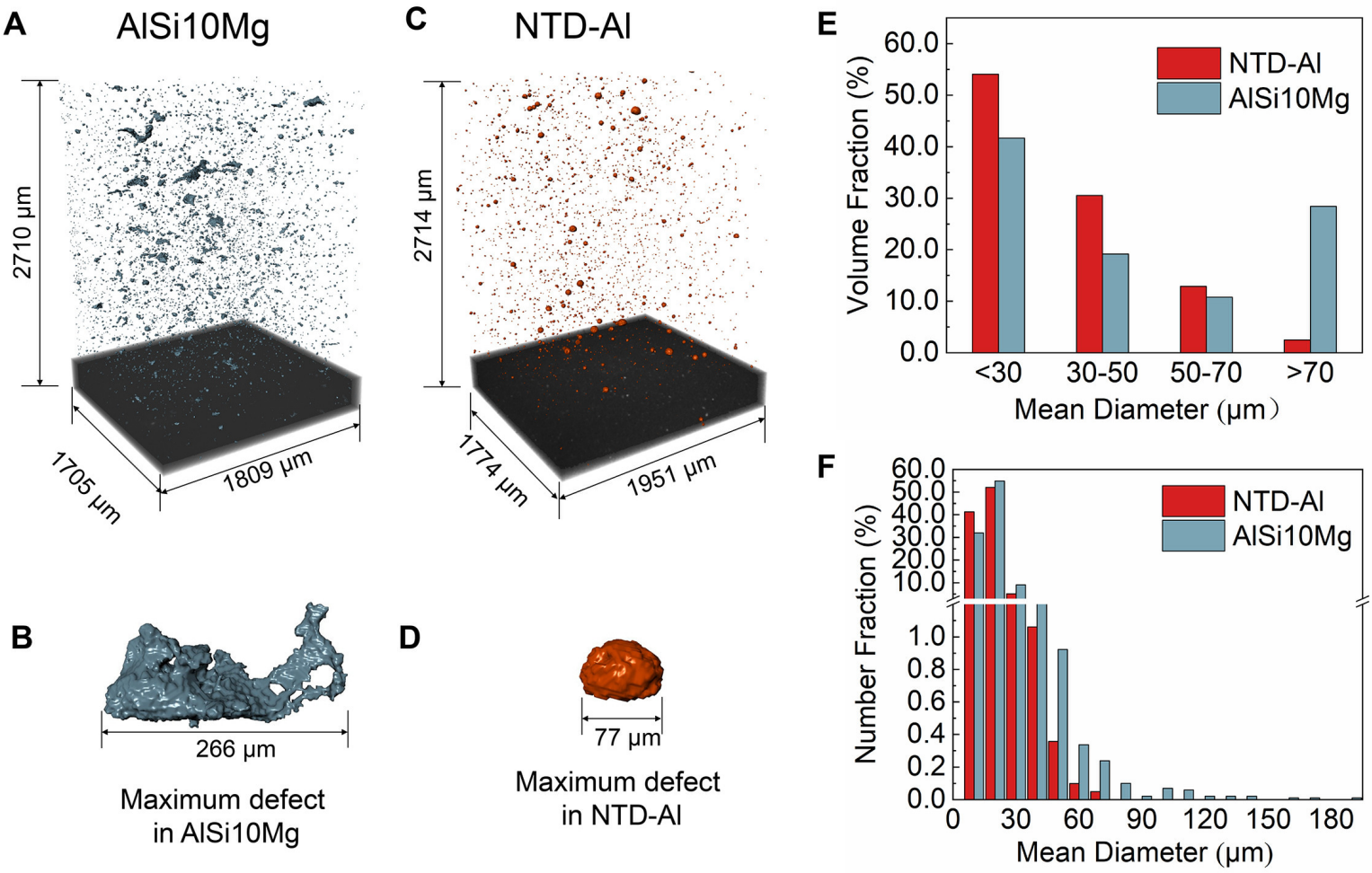
A
AlSi10Mg
2710 μm
1705 μm
1809 μm
B
266 μm
Maximum defect
in AlSi10Mg
C
NTD-Al
2714 μm
1774 μm
1951 μm
D
77 μm
Maximum defect
in NTD-Al
E
Volume Fraction (%)
60.0
50.0
40.0
30.0
20.0
10.0
0.0
NTD-Al
AlSi10Mg
<30
30-50
50-70
>70
Mean Diameter (μm)
F
Number Fraction (%)
60.0
50.0
40.0
30.0
20.0
10.0
1.0
0.8
0.6
0.4
0.2
0.0
NTD-Al
AlSi10Mg
0
30
60
90
120
150
180
Mean Diameter (μm)

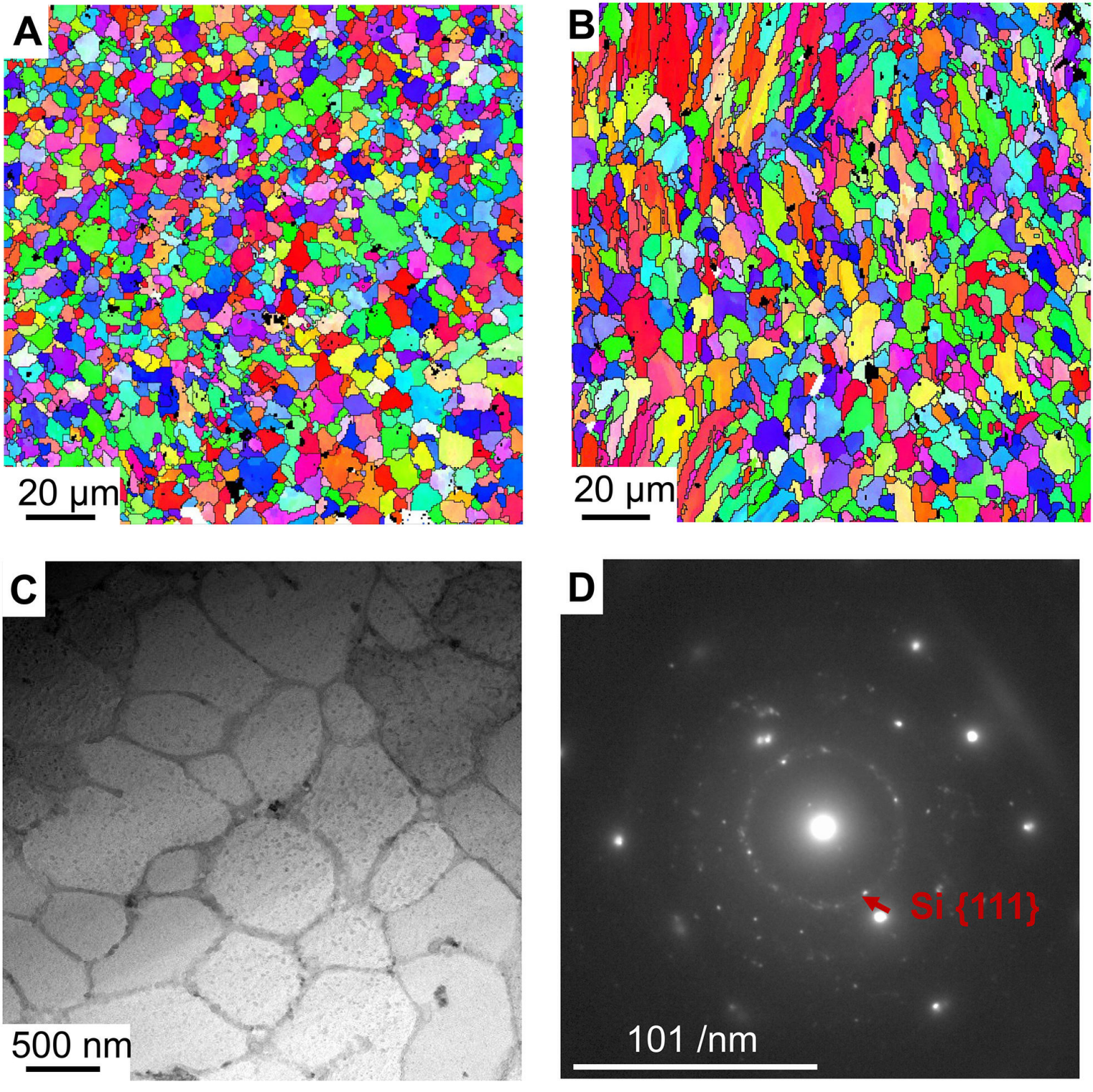
A
20 μm
B
20 μm
C
500 nm
D
Si {111}
101 /nm

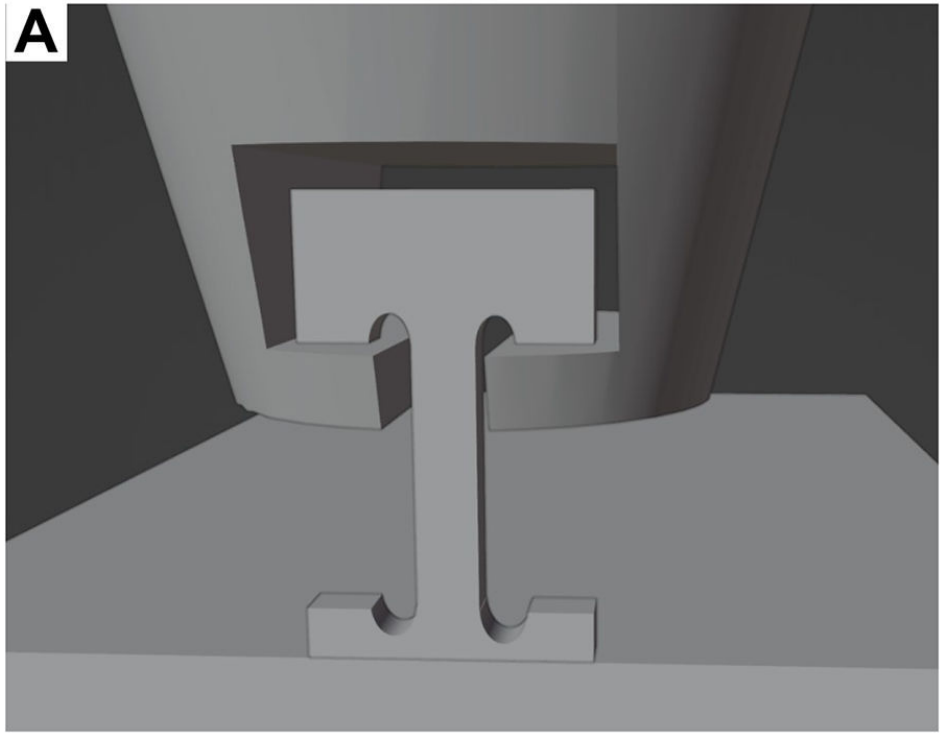
A

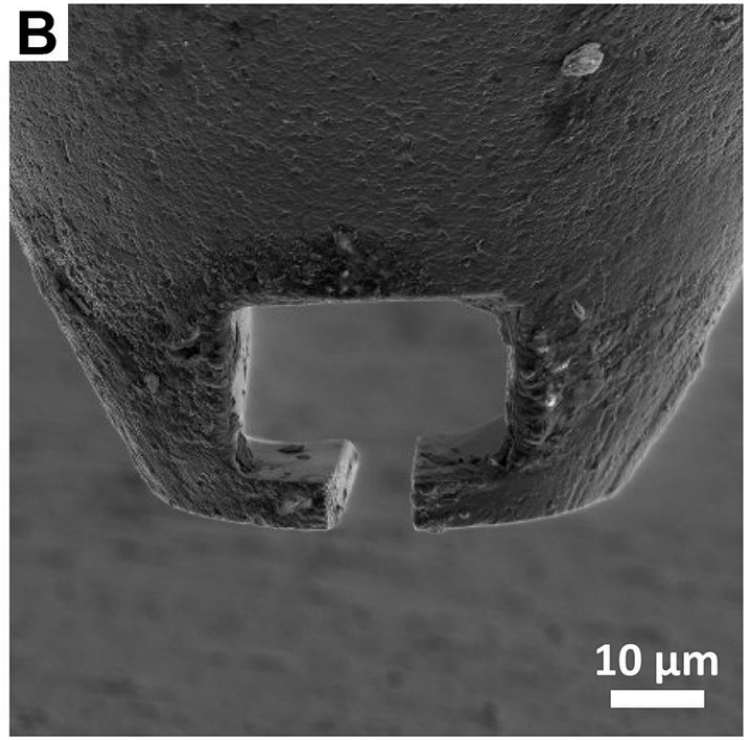
B
10 µm

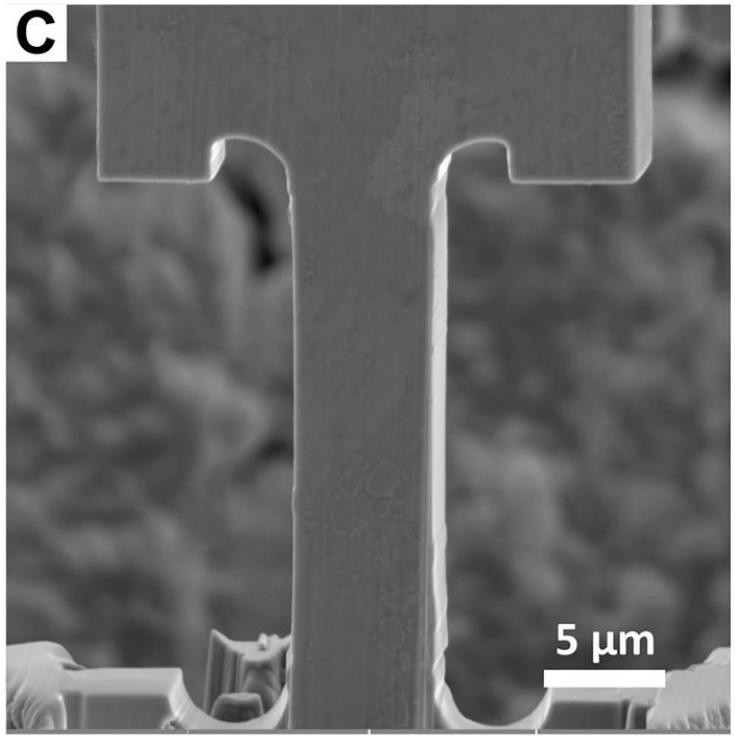
C
5 µm

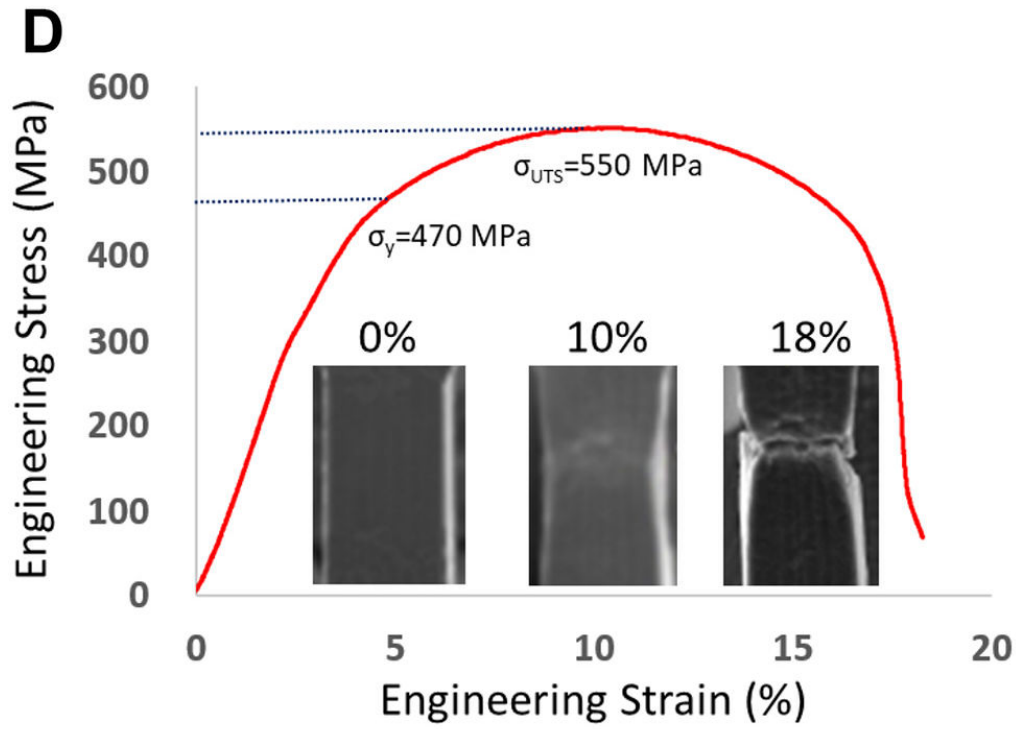
D
Engineering Stress (MPa)
600
500
400
300
200
100
0
0
5
10
15
20
Engineering Strain (%)
σUTS=550 MPa
σy=470 MPa
0%
10%
18%

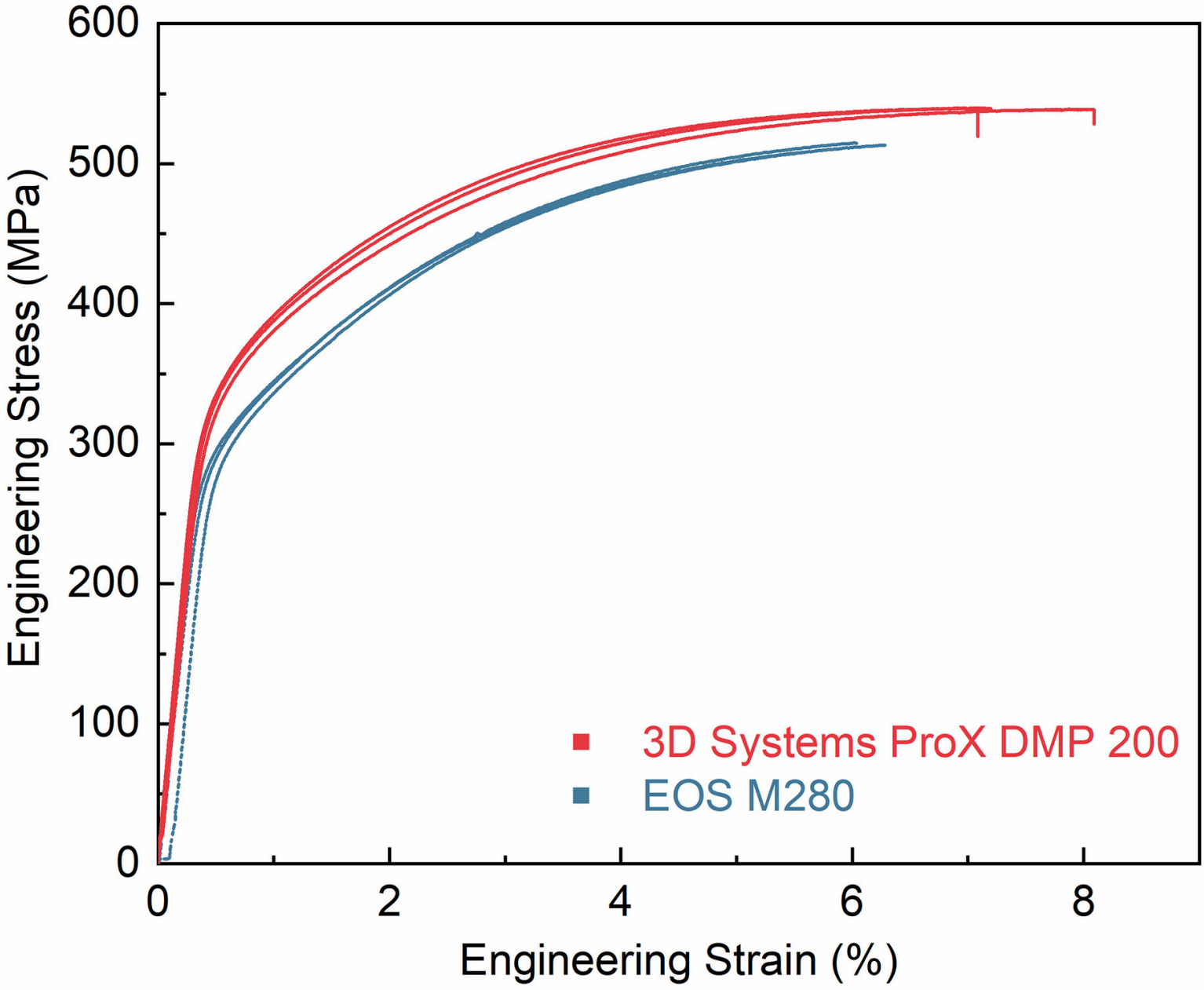
600
500
400
300
200
100
0
Engineering Stress (MPa)
0
2
4
6
8
Engineering Strain (%)
3D Systems ProX DMP 200
EOS M280

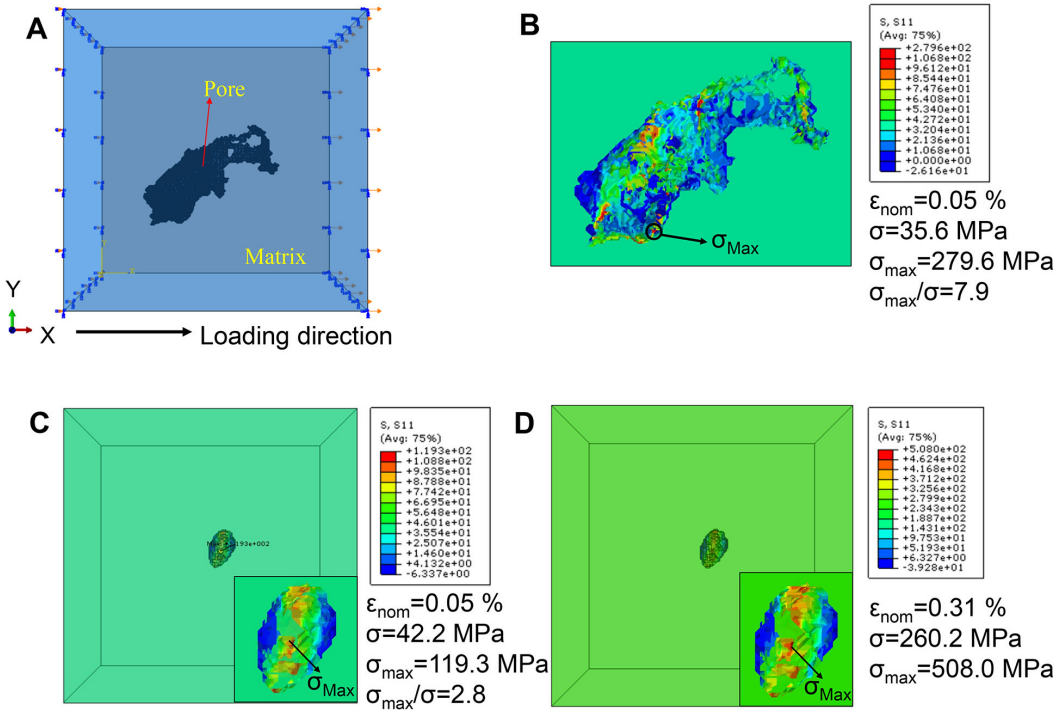


E

| | | | | | | | | | |
|---|---|---|---|---|---|---|---|---|---|
| Defects in AlSi10Mg alloy | 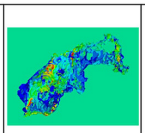 | 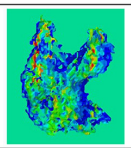 | 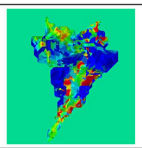 | 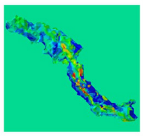 | 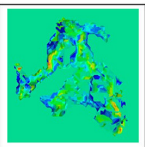 | 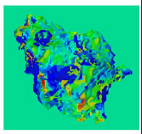 | 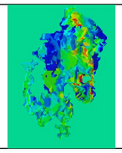 | 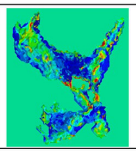 | 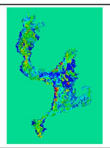 |
| Stress concentration factor | 7.9 | 6.1 | 7.3 | 6.2 | 5.2 | 7.8 | 7.7 | 7.0 | 4.3 |
| Pores in NTD-Al alloy | 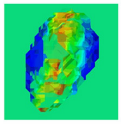 | 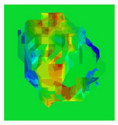 | 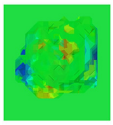 | 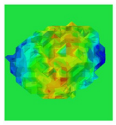 | 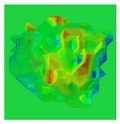 | 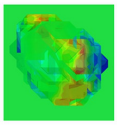 | 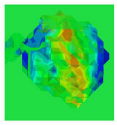 | 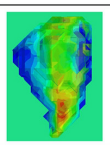 | 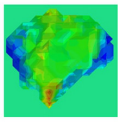 |
| Stress concentration factor | 2.8 | 2.4 | 2.3 | 2.3 | 2.2 | 2.3 | 2.5 | 3.0 | 2.8 |

Loading direction

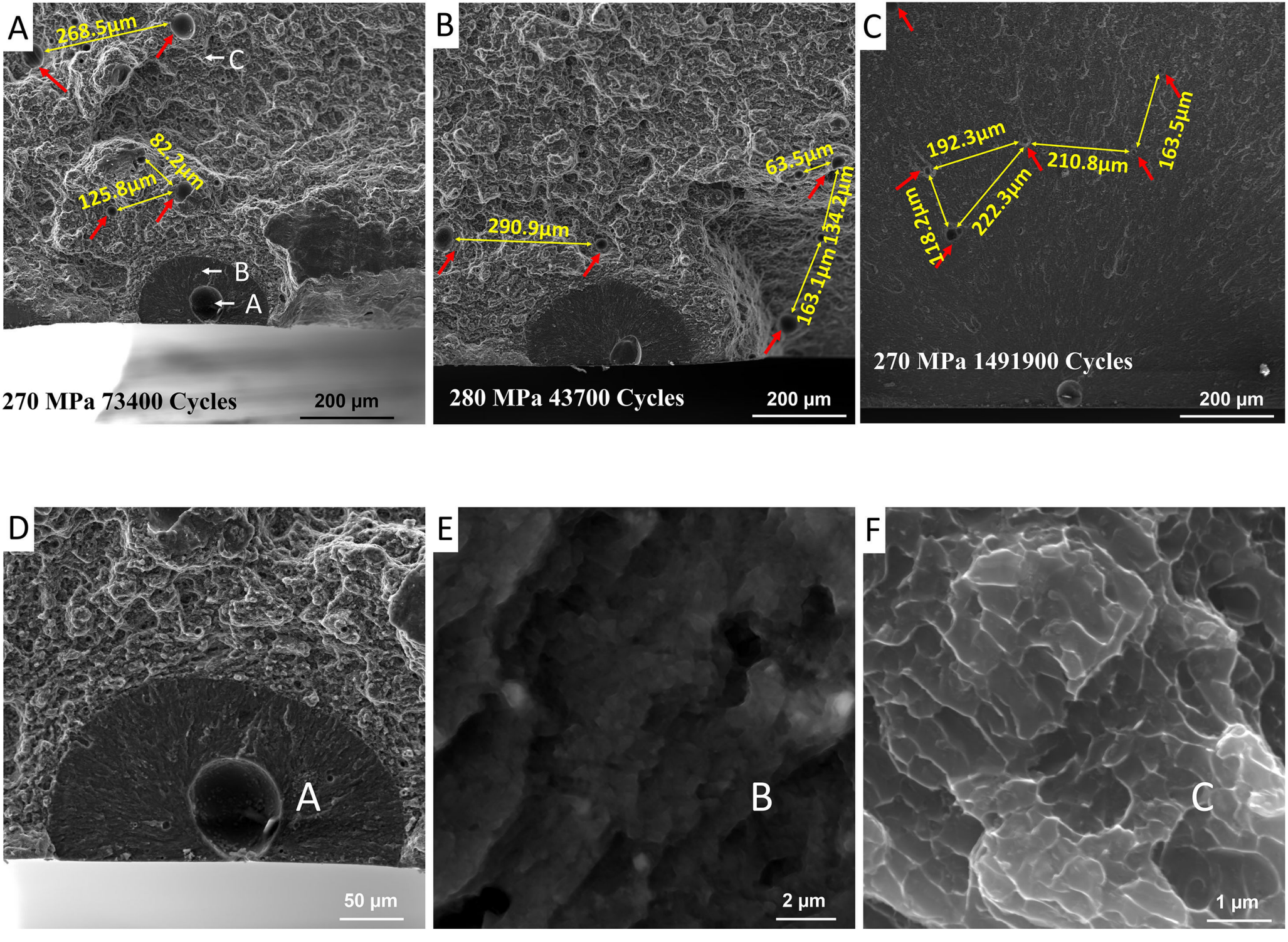
A
268.5μm
C
82.2μm
125.8μm
B
A
270 MPa 73400 Cycles
200 μm
B
63.5μm
290.9μm
134.2μm
163.1μm
280 MPa 43700 Cycles
200 μm
C
192.3μm
210.8μm
163.5μm
222.3μm
118.2μm
270 MPa 1491900 Cycles
200 μm
D
A
50 μm
E
B
2 μm
F
C
1 μm

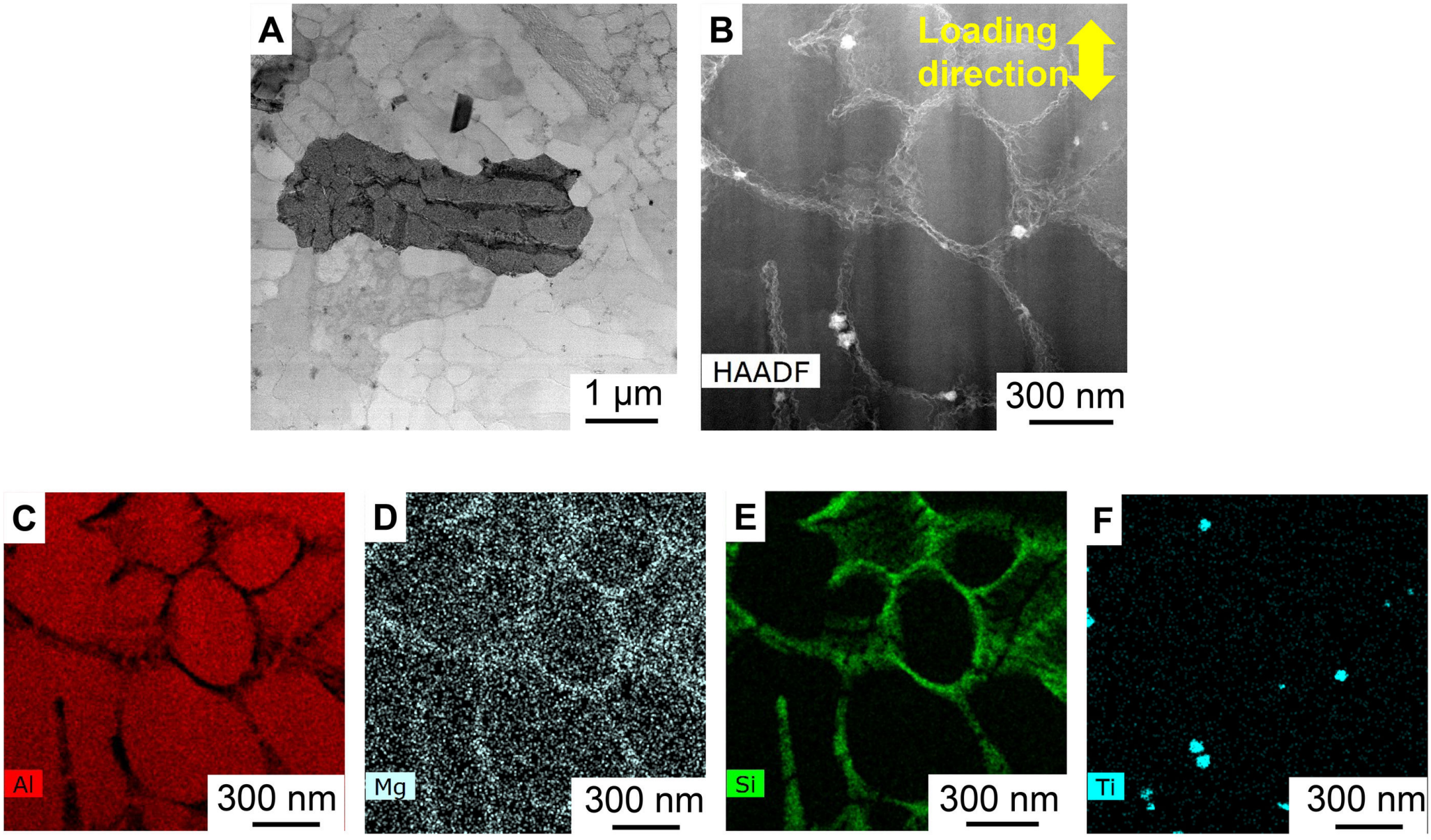
A
1 μm
B
Loading direction
HAADF
300 nm
C
Al
300 nm
D
Mg
300 nm
E
Si
300 nm
F
Ti
300 nm